

TECHNICAL REPORT STANDARD PAGE

1. Report No. FHWA/LA.10/471		2. Government Accession No.	3. Recipient's Catalog No.
4. Title and Subtitle Evaluation of the Base/Subgrade Soil under Repeated Loading: Phase II– In-Box and ALF Cyclic Plate Load Tests		5. Report Date March 2012	
		6. Performing Organization Code LTRC Project Number: 05-5GT State Project Number: 736-99-1312	
7. Author(s) Murad Y. Abu-Farsakh, Ph.D., P.E., and Qiming Chen, Ph.D., P.E.		8. Performing Organization Report No.	
9. Performing Organization Name and Address Louisiana Transportation Research Center 4101 Gourrier Avenue Baton Rouge, LA 70808		10. Work Unit No.	
		11. Contract or Grant No. LTRC Number: 05-5GT State Project Number: 736-99-1312	
12. Sponsoring Agency Name and Address Louisiana Transportation Research Center 4101 Gourrier Avenue Baton Rouge, LA 70808		13. Type of Report and Period Covered Final Report – Phase II Aug 2005 - June 2010	
		14. Sponsoring Agency Code	
15. Supplementary Notes Conducted in Cooperation with the U.S. Department of Transportation, Federal Highway Administration			
16. Abstract This research study aims at evaluating the performance of base and subgrade soil in flexible pavements under repeated loading test conditions. For this purpose, an indoor cyclic plate load testing equipment was developed and used to conduct a series of large-scale in-box tests and full-scale field tests on several pavement sections. The in-box cyclic plate load tests were conducted to evaluate the performance and benefits of geogrid base reinforcement in flexible pavements. A total of 12 tests were performed on unreinforced and geogrid-reinforced pavement sections. The parameters investigated in this study included the aperture shape (geometry) of the geogrid, location of the geogrid within the base layer, and geogrid tensile modulus. The stress distribution and permanent vertical strain in the subgrade, the development of excess pore water pressure in the subgrade, and the strain distribution along the geogrids were also investigated. The test results showed that the inclusion of geogrids can significantly improve the performance of flexible pavements on weak subgrades [California Boring Ratio (CBR) \leq 1%], and that the traffic benefit ratio (TBR) can be increased up to 15.3 at a rut depth of 0.75 in. (19 mm). Better performance was observed when the geogrid was placed within the upper one third of the base aggregate layer. The inclusion of geogrid helps redistribute the applied surface load to a wider area on top of the subgrade layer, thus reducing the accumulated permanent deformation within the subgrade. Full-scale field tests were also conducted on several test lane sections built at the Pavement Research Facility (PRF) site using two types of loadings: cyclic plate load test and rolling wheel load test. These sections include blended calcium sulfate (BCS), stabilized BCS, stabilized recycled asphalt pavement (RAP), and stabilized soil as base/subbase materials. The differences in pavement responses of the tested sections to cyclic plate and rolling wheel loads were investigated. The measured rut depth caused by rolling wheel load, in all test sections, were much higher than those measured from the cyclic plate load test. The difference can be as much as 3 to 7 times between these two types of loading. This is mainly due to the effects of principal stress rotation and lateral wander on the permanent deformation of pavements. The field test results also indicate that the cyclic plate load test can be a good performance indicator test for the evaluation and pre-selection of pavement sections for field tests.			
17. Key Words		18. Distribution Statement Unrestricted. This document is available through the National Technical Information Service, Springfield, VA 21161.	
19. Security Classif. (of this report) Unclassified	20. Security Classif. (of this page) Unclassified	21. No. of Pages 97	22. Price

Evaluation of the Base/Subgrade Soil under Repeated Loading

by

Murad Y. Abu-Farsakh, Ph.D., P.E.

Qiming Chen, Ph.D., P.E.

Louisiana Transportation Research Center

4101 Gourrier Avenue

Baton Rouge, LA 70808

LTRC Project No. 05-5GT

State Project No. 736-99-1312

conducted for

Louisiana Department of Transportation and Development

Louisiana Transportation Research Center

The contents of this report reflect the views of the author/principal investigator who is responsible for the facts and the accuracy of the data presented herein. The contents do not necessarily reflect the views or policies of the Louisiana Department of Transportation and Development or the Louisiana Transportation Research Center. This report does not constitute a standard, specification, or regulation.

March 2012

Project Review Committee

Each research project will have an advisory committee appointed by the LTRC Director. The Project Review Committee is responsible for assisting the LTRC Administrator or Manager in the development of acceptable research problem statements, requests for proposals, review of research proposals, oversight of approved research projects, and implementation of findings.

LTRC appreciates the dedication of the following Project Review Committee Members in guiding this research study to fruition.

LTRC Administrator

Zhongjie “Doc” Zhang, Ph.D., P.E.
Pavement and Geotechnical Research Administrator

Members

Jeff Lambert, LADOTD
Kim Garlington, LADOTD
Steve Draughon, LADOTD
Philip Arena, FHWA
Nicholas Reck, Earth Technologies, Inc.
Masood Rasoulilian, LADOTD
Mike Boudreaux, LTRC
Sam Cooper, LTRC
Bailey Williams, Vulcan

Directorate Implementation Sponsor

Richard Savoie, P.E.
DOTD Chief Engineer

ABSTRACT

This research study aimed at evaluating the performance of base and subgrade soil in flexible pavements under repeated loading test conditions. For this purpose, an indoor cyclic plate load testing equipment was developed and used to conduct a series of large-scale in-box tests and full-scale field tests on several pavement sections.

The in-box cyclic plate load tests were conducted to evaluate the performance and benefits of geogrid base reinforcement in flexible pavements. A total of 12 tests were performed on unreinforced and geogrid-reinforced pavement sections. The parameters investigated in this study included the aperture shape (geometry) of the geogrid, location of the geogrid within the base layer, and geogrid tensile modulus. The stress distribution and permanent vertical strain in the subgrade, the development of excess pore water pressure in the subgrade, and the strain distribution along the geogrids were also investigated. The test results showed that the inclusion of geogrids can significantly improve the performance of flexible pavements on weak subgrades [California Boring Ratio (CBR) $\leq 1\%$], and that the traffic benefit ratio (TBR) can be increased up to 15.3 at a rut depth of 0.75 in. (19 mm). Better performance was observed when the geogrid was placed within the upper one third of the base aggregate layer. The inclusion of geogrid helps redistribute the applied surface load to a wider area on top of the subgrade layer, thus reducing the accumulated permanent deformation within the subgrade.

Full-scale field tests were also conducted on several test lane sections built at the Pavement Research Facility (PRF) site using two types of loadings: cyclic plate load test and rolling wheel load test. These sections include blended calcium sulfate (BCS), stabilized BCS, stabilized recycled asphalt pavement (RAP), and stabilized soil as base/subbase materials. The differences in pavement responses of the tested sections to cyclic plate and rolling wheel loads were investigated. The measured rut depth caused by rolling wheel load, in all test sections, were much higher than those measured from the cyclic plate load test. The difference can be as much as 3 to 7 times between these two types of loading. This is mainly due to the effects of principal stress rotation and lateral wander on the permanent deformation of pavements. The field test results also indicate that the cyclic plate load test can be a good performance indicator test for the evaluation and pre-selection of pavement sections for field tests.

ACKNOWLEDGMENTS

This research project was funded by the Louisiana Department of Transportation and Development (LADOTD) (State Project No. 736-99-1312) and the Louisiana Transportation Research Center (LTRC Project No. 05-5GT). The comments and suggestions of Mark Morvant, associate director of research; Zhongjie “Doc” Zhang, pavement and geotechnical administrator; and Gavin Gautreau, geotechnical engineering manager, of LTRC are gratefully acknowledged. The authors want to extend their thanks to William Tierney, Benjamin Comeaux, and Amar Raghavendra for providing valuable assistance in this study. The help from the pavement research section and Accelerated Load Facilities (ALF) personnel is also greatly appreciated.

IMPLEMENTATION STATEMENT

An indoor cyclic plate load testing equipment was developed for the purpose of evaluating the performance of base and subgrade soil in flexible pavement sections under repeated loading test conditions. In this study, the testing equipment was used to conduct an in-box large-scale testing program to characterize the performance of geogrid base reinforcement in flexible pavements and to evaluate the effect of different variables and parameters contributing to geogrid benefits. A full-scale field testing program was also conducted at the PRF site to evaluate and compare the performance of different base/subbase materials under two different types of loading: cyclic plate load test and rolling wheel load test. In addition, the research study included laboratory testing to evaluate the performance of geogrid reinforced base course specimens using the material test system (MTS) machine and performing finite element parametric analyses to investigate the benefits of geogrid base reinforcement in flexible pavement structures (published in Final Report No. 450 [1]).

The results of this study demonstrated the potential benefits of geogrid base reinforcement of aggregate layers in flexible pavements through the improvement of the strength/stiffness of the base course material and protecting/stabilizing the subgrade layer, thus reducing the pavement's permanent deformation (rutting) and fatigue cracking under cyclic loading. The geogrid benefits were identified to be a function of base layer thickness, geogrid modulus, location and geometry, and subgrade strength.

The findings of this research study can be implemented in the design of flexible pavements built on top of weak subgrades with resilient modulus $M_r < 2000$ psi (13,790 kPa) by reinforcing the base aggregate layers with one or two layers of geogrids, especially in cases where it is difficult to stabilize/treat the soft subgrade soil with cement or lime. The use of geogrids with elastic tensile strength at 2 percent strain, $T_{2\%} \geq 250$ lb/ft (3.65 kN/m), is recommended.

One layer of geogrid reinforcement should be placed at the base-subgrade interface for pavements with a base thickness less than 18 in. (457.2 mm) built on top of a weak subgrade. For base thicknesses equal or greater than 18 in. (457.2 mm), two geogrid layers are recommended, one layer to be placed at the base-subgrade interface and another geogrid layer at the upper one third of the base aggregate layer.

The geogrid base reinforcement/subgrade stabilization can also be implemented to create working platforms for construction of pavements and embankments on top of soft soils. Where proper design dictates, the geogrid layer should be placed on top of soft subgrade immediately above the geotextile layer.

One promising application of geogrids (and high strength geotextiles) is for use in widening existing roadways through stabilizing weak subgrade layers. The inclusion of geogrid/geotextile layer at the base-subgrade interface will enhance the bearing capacity of the subgrade layer, increases its resistance to shear failure, and help eliminate the differential settlement between the existing and new lanes. The DCP test can be used to evaluate the strength condition and resilient modulus of the subgrade soil for use as input parameters in the design the new pavement lane section.

The results of this study indicated that the cyclic plate load test can be used as a good performance indicator test for evaluating the unpaved and paved test sections. Accordingly, the researchers recommend using the in-box cyclic plate load testing equipment for comparing the performance of different pavement sections and for pre-selection of pavement sections for further full-scale field testing, especially when the load-related performance of new pavement materials and concepts are needed to be evaluated and approved.

The researchers also recommend using the proposed modified equivalent formula to calculate the equivalent modulus of elasticity, which considers both the thickness and relative position of individual layers, in the design and analysis of pavements when multiple-layers have to be combined from a practical standpoint.

TABLE OF CONTENTS

ABSTRACT.....	iii
ACKNOWLEDGMENTS	v
IMPLEMENTATION STATEMENT	vii
TABLE OF CONTENTS.....	ix
LIST OF TABLES	xi
LIST OF FIGURES	xiii
INTRODUCTION	1
Background.....	1
Literature Review.....	3
Geogrid Base Reinforcement.....	3
Cyclic Plate Load Tests versus Rolling Wheel Load Tests	4
OBJECTIVE	7
SCOPE	9
METHODOLOGY	11
Development of an Indoor Cyclic Plate Load Test.....	11
Laboratory Cyclic Plate Load Tests.....	14
Test Equipment	14
Pavement Layer Materials	14
Testing Program and Sample Preparation Techniques	17
Instrumentation Program	21
Field Cyclic Plate Load and Rolling Wheel Load Tests.....	26
Test Facilities	26
Pavement Test Sections	28
Pavement Layer Materials	30
DISCUSSION OF RESULTS.....	33
Evaluation of Geogrid Base Reinforcement Using Cyclic Plate Load Testing	33
Test Results.....	33
Surface Deformation and Contour	40
Effect of Properties and Type of Geogrid.....	43
Effect of Location of Geogrid.....	43
Stress Distribution and Vertical Permanent Strain within Subgrade	45
Strain Distribution along the Geogrid.....	47
Pore Water Pressure within Subgrade.....	51
General Comments.....	52
Field Load Tests on Various Base/Subbase Materials.....	54

Test Results.....	54
Comparison of Various Sections	58
Cyclic Plate Load Tests versus Rolling Wheel Load Tests	61
General Comments.....	66
CONCLUSIONS.....	67
Evaluation of Geogrid Base Reinforcement Using Cyclic Plate Load Test	67
Field Tests on Various Base/Subbase ALF Test Lanes	69
RECOMMENDATIONS	71
ACRONYMS, ABBREVIATIONS, AND SYMBOLS	73
REFERENCES	75

LIST OF TABLES

Table 1 Properties of geogrids	15
Table 2 Combination of base/subbase materials in pavement test sections.....	29
Table 3 Properties of base materials	31
Table 4 Properties of subbase and subgrade materials	31
Table 5 In-place properties of subgrade.....	34
Table 6 In-place properties of base course	35
Table 7 In-place properties of HMA.....	36
Table 8 Summary of cyclic plate load tests	37
Table 9 In-place properties	56
Table 10 Equivalent modulus of elasticity of base and subbase layer.....	60
Table 11 The ratio of rut depth for rolling wheel load test to that for cyclic plate load test ..	61

LIST OF FIGURES

Figure 1 Schematic of the indoor cyclic plate load test equipment	12
Figure 2 Image of the indoor cyclic plate load test equipment.....	12
Figure 3 Schematic of the field cyclic plate load test equipment	13
Figure 4 Image of the field cyclic plate load test equipment.....	13
Figure 5 Laboratory test box, hydraulic actuator, and reaction system	16
Figure 6 Load pulse applied in the test	16
Figure 7 Placement of soil strain gauge	18
Figure 8 Placement of piezometers.....	19
Figure 9 Placement of pressure cells	19
Figure 10 Placement of geogrids with strain gages	20
Figure 11 Preparation of the AC layer	20
Figure 12 Schematic of the indoor test box for cyclic load testing	21
Figure 13 Data acquisition system.....	24
Figure 14 Cyclic plate load testing equipment	27
Figure 15 Load pulse applied in the test	27
Figure 16 Rolling wheel load testing facility.....	28
Figure 17 Plan layout of testing sections (not to scale)	29
Figure 18 Pavement structure of testing sections (not to scale).....	29
Figure 19 Development of surface permanent deformation for different types of geogrid placed at base/subgrade interface	38
Figure 20 Development of surface permanent deformation for GG3 and GG4 geogrids placed at different locations.....	38
Figure 21 Development of surface permanent deformation for GG4 geogrid placed at the middle of base layer with and without prime coat	39
Figure 22 Development of surface permanent deformation for unreinforced weak and strong sections and GG4 reinforced section.....	39
Figure 23 Typical response of pressure cells.....	41
Figure 24 Typical response of strain gauge	42
Figure 25 Profile of surface deformation at N = 30,000.....	42
Figure 26 Possible configurations at the geogrid interface.....	45
Figure 27 Vertical stress distribution at N = 30,000 [at 3 in. (76 mm) below the top of subgrade]	46
Figure 28 Permanent vertical strain in the subgrade versus load cycle [at 3 in. (76 mm) below the top of subgrade].....	47
Figure 29 Permanent strain distribution along the centerline of GG1 geogrid placed at the	

base/subgrade interface (<i>D</i> : loading plate diameter)	48
Figure 30 Permanent strain distribution along the centerline of GG2 geogrid placed at the base/subgrade interface (<i>D</i> : loading plate diameter)	49
Figure 31 Permanent strain distribution along the centerline of GG3 geogrid placed at the base/subgrade interface (<i>D</i> : loading plate diameter)	50
Figure 32 Permanent strain distribution along the centerline of GG3 geogrid placed at the middle of base layer (<i>D</i> : loading plate diameter)	50
Figure 33 Permanent strain distribution along the centerline of GG4 geogrid placed at the middle of base layer (<i>D</i> : loading plate diameter)	51
Figure 34 Development of pore water pressure and amplitude of cyclic surface deformation at the center	53
Figure 35 Development of rut depth for repeatability check	56
Figure 36 Comparison of field and laboratory cyclic plate load test	57
Figure 37 Development of rut depth for cyclic plate load test	57
Figure 38 Development of rut depth for rolling wheel load test.....	58
Figure 39 Stress regimes experienced by pavement element under two types of loading	63
Figure 40 Variation of the resilient modulus M_r with time.....	65

INTRODUCTION

Background

The United States of America owns the largest highway system in the world with more than 3.9 million miles (62.4 million kilometers) of roads as of 2004. The highway volume reached around 2.7 trillion vehicle-miles (4.32 trillion vehicle-kilometers) in 2000, which is equivalent to about 7.4 billion vehicle-miles (11.84 billion vehicle-kilometers) of travel every day. The equivalent truck travel (single-unit and combinations) had increased by 231 percent from 1970 to 2004, while the combination truck travel had increased by 285 percent to account for 4.9 percent of the total annual vehicle-miles of travel versus 3.2 percent in 1970 [2]. In order to meet the future challenges for better and durable highway pavement design and maintenance, a cost-effective accelerated testing facility is therefore needed to test new highway materials, recycled materials, different subgrade conditions, and/or new design methodology. The Louisiana Transportation Research Center (LTRC) possesses the state of the art Accelerated Load Facility (ALF) located at the Pavement Research Facility (PRF) site. This facility has been used extensively for full-scale pavement testing applications of different materials and pavement conditions. However, due to the large size of the facility, long test duration time, and the associated high cost, a limited number of pavement lanes can be tested in a year. Therefore, an indoor large-scale cyclic plate load testing facility that is capable of simulating the vehicular loading has been developed. The new in-box actuator testing facility can be used for testing pavement sections of different base materials, different subgrade conditions, different cross sections, and different loading conditions, as well as, the possibility for using it for other pavement and geotechnical applications such as testing new materials/products, new stabilizing techniques, and new design methodologies. In this study, the cyclic plate load testing equipment was used in the box to evaluate the performance and benefits of geogrid reinforcement in a flexible pavement system and to evaluate and compare the performance of several full-scale test lane sections built at the PRF site with the rolling wheel accelerated load testing.

Due to the nature of Louisiana soils, in many cases, pavements have to be built over soft subgrade soils, which is often associated with design and construction difficulties. The design of flexible pavements over weak subgrades has been always a challenge for pavement design engineers. The traditional solution to this problem is to replace part of the subgrade with base course aggregate and/or treating/stabilizing the subgrade with cement or lime. The purpose is to create a working platform through improving the engineering properties of the subgrade. The use of geosynthetics (mainly geogrids) to reinforce the base aggregate layer within a pavement structure can offer a cost-effective alternative solution to this problem. The

attraction of using geogrid base reinforcement lies in the possibility of extending the pavement's service life, reducing the base course thickness for a given service life, delaying rutting development, and helping construction of pavements over soft subgrades [3, 4, 5, 6, 7, 8]. Although the benefits of geogrid base reinforcement in flexible pavements have been well realized, there is no acceptable design methodology for inclusion the geosynthetic benefits in a nationally recognized design method, such as the Mechanistic-Empirical Pavement Design Guide (MEPDG) [2]. The AASHTO 1993 and the MEPDG methods did not incorporate the geogrid base reinforcement in flexible pavement design due to the lack of understanding the actual mechanisms of geogrid reinforcement, especially rigorously quantifying the geogrid benefits [2]. These limitations provide a motivation for continual research efforts on geogrid reinforced pavement sections so that the benefits of geogrid reinforcement can be included in the future into pavement design methods. Undoubtedly, a successful instrumentation program is necessary to achieve this goal.

Given the complex nature of a geogrid reinforced flexible pavement and the introduction of new variables associated with the reinforcement, a mechanistic procedure is needed for providing a design procedure expressed in terms of material properties of the pavement layers (asphalt concrete, base, and subgrade) and the geogrid materials composing the pavement system. In order to develop such mechanistic design procedures for reinforced pavement structures, a better understanding and characterization of the geogrid reinforced mechanisms should be established. In addition, the factors that affect the geogrid reinforced pavement structure should be investigated and evaluated.

This study aimed at evaluating the benefits of geogrid base reinforcement of the base course aggregate layer in a flexible pavement structure through conducting extensive experimental testing and numerical modeling programs. The experimental testing included small-scale laboratory testing of geogrid reinforced base aggregate specimens and large-scale in-box cyclic plate load testing of geogrid reinforced pavement sections. The numerical modeling included finite element analyses to evaluate the effect of geogrid stiffness and location, thickness of the base course layer, and strength of the subgrade material on the performance of geogrid reinforced flexible pavement structures.

The cyclic plate load testing equipment was also deployed to the PRF site to evaluate the performance of full-scale test lane sections (no geogrid was used in any of these sections). Pavement sections with different base and subbase materials were tested. This included testing six types of base material [raw BCS, class C flyash stabilized BCS, 120 grade ground granulated blast furnace slag (GGBFS) stabilized BCS, foamed asphalt (FA) stabilized RAP, and FA stabilized RAP and soil cement blend] and two types of subbase materials (including

lime and cement treated soil). The pavement response from cyclic plate load tests was compared with the results of rolling wheel accelerated load testing for validation and verifications.

This report will present the results of large-scale testing on geogrid base reinforced pavement sections and full-scale testing on PRF test sections. The results of small-scale testing and finite element numerical modeling were presented earlier in Final Report 450 [1].

Literature Review

Geogrid Base Reinforcement

The use of geogrid reinforcement in roadway applications started in the 1970s. Since then, the technique of geogrid reinforcement has been increasingly used and many studies have been performed to investigate the behavior of geogrid reinforcement in roadway applications [10, 11, 12, 13, 14, 15]. The results of experimental, analytical, and numerical studies reported in literature showed that geogrid reinforcement in pavement structures can extend the pavement's service life, reduce base course thickness for a given service life, delay rutting development and help construction of pavements over soft subgrades [3, 4, 5, 6, 7, 8].

The amount of improvement in pavement performance with the inclusion of geogrid in the base course layer depends on many factors, including the strength of subgrade, geogrid properties, location of geogrid in the pavement, thickness of base course layer, etc. Previous studies have shown that the weaker the subgrade, the higher the percent reduction of rutting, while little improvement obtained for subgrades with high CBR values [4,12]. Another factor that plays an important role in the performance of geogrid base-reinforced pavement is the thickness of the base course layer. The benefit of a geogrid generally decreases with an increase in the thickness of the base course and becomes insignificant when the base course is very thick [8, 16].

The location of geogrid(s) within the base course layer in the pavement system is very important to its reinforcement effectiveness [12, 17]. The optimum location of a geogrid depends on many factors, such as subgrade strength and base course thickness. Al-Qadi et al. concluded that for a thin base course layer, placing a geogrid layer at the subgrade/base course interface gives better performance and that the geogrid layer should be placed at the upper one third of the base course layer for a thicker base course layer [18]. This finding is in agreement with the work of Hass et al. [10]. However, Hass et al. also concluded that no benefits were achieved when a single layer of geogrid was placed at the midpoint or higher within a thick base course layer over very soft flexible subgrades [10].

The improved performance of geogrid reinforcement in flexible pavements also depends on the properties of the geogrid, such as aperture geometry, stability modulus, flexural stiffness, junction strength, and tensile modulus. However, the current available information does not provide clear quantifiable values for any of these properties [15]. It is believed that these properties work together to determine the performance of a geogrid in a pavement system. Any property alone may not be enough to characterize the performance of a geogrid.

As manifested in these previous studies, the reinforcement effectiveness of the geogrid in a pavement system and the rational design of geogrid base-reinforced pavements are contingent upon properly considering the combined effect of all influencing factors. To this end, pavement response under cyclic loading has often been monitored with a well-planned and executed instrumentation program. The success of an instrumentation program depends on the selection of appropriate sensors, wise selection of their locations, and proper preparation and installation of the instruments.

Van Deusen et al. presented a comprehensive review of instrumentation practices for the measurement of stresses, strains, and deflections in pavement structures [19]. They found that the simplest possible installation procedures minimize inconsistencies in the results due to placement errors. Perkins implemented an extensive instrumentation program to study the performance of geosynthetics reinforced flexible pavements [12]. The measured stress and strain data revealed a significantly different response between reinforced and unreinforced sections. These data provided insight into the reinforcement mechanism of geogrid base reinforcement and could lead to a significant improvement in the design of geogrid reinforced pavement systems.

Cyclic Plate Load Tests versus Rolling Wheel Load Tests

Based on results obtained from full-scale tests, Brown and Brodrick showed that the rut depths of pavement sections under the rolling wheel loads were consistently higher than those under the cyclic plate loads [20]. The difference can be as much as 3 ~ 4 times between these two types of loading. Based on the results of the cyclic plate load test and rolling wheel load test on two instrumented low traffic pavement sections, Hornyk et al. reported that the permanent strains in the base layer under the rolling wheel load were about three times higher than those measured under the cyclic plate load [21].

The inherent difference between the cyclic plate and rolling wheel load tests is such that in the rolling wheel load tests a pavement element within the plane of the wheel track experiences a continuous rotation of the principal stress. The studies available in literature have shown that the principal stress rotation has a significant and deleterious impact on the permanent deformation of both asphalt concrete and base/subbase materials [22, 23, 24, 25].

For example, the results of the experimental study by Grabe and Clayton indicated that the rate of permanent strain increase with principal stress rotation can be 3.8 times as high as that without principal stress rotation [25].

Lateral wander was also considered in the rolling wheel load tests of this study. Most lateral wander effect studies available in the literature focused on the HMA [26 and 27]. The findings of those studies generally led to the conclusion that the rut depth for the rolling wheel load with wander is less than that for the channelized rolling wheel load at a given number of wheel passes because the loading time on any given wheel path was reduced with wander [28]. However, a recent interesting research study by Donovan and Tutumluer found that the load wander resulted in a dramatic degradation of the unbound aggregate layer [29]. They attributed this degradation to the recurring movement and rearrangement of the particles, which gradually reduces the strength of the unbound materials and thus cause more permanent deformation with future load applications. They referred to this effect as the “anti-shakedown” effect.

OBJECTIVE

The main objective of this study was to evaluate the performance of different base/subbase materials under different types of loading and to investigate the potential benefits of using geogrid base reinforcement in pavement systems. These include:

- (1) Develop an indoor cyclic load testing equipment for testing of paved/unpaved roads and pre-selection and screening of pavement sections for recommendation of further full-scale field test sections.
- (2) Conduct large-scale in-box experimental testing to investigate the influence of subgrade strength and the reinforcement type and stiffness on the base reinforcement benefits.
- (3) Validate the results of the cyclic load actuator by comparing the pavement response under cyclic plate loading with that of rolling wheel loading on full-scale ALF test sections.
- (4) Conduct a finite element parametric study on the effect of different variables and parameters contributing to the improved performance of flexible pavement with geogrid base reinforcement.

SCOPE

The stated objectives of this research study were achieved through conducting both experimental testing and numerical modeling programs. The experimental testing program included conducting large-scale in-box cyclic plate load testing on geogrid base-reinforced pavement sections, full-scale cyclic plate load testing on several ALF test sections, and small-scale laboratory triaxial testing on geogrid reinforced base aggregate specimens. The numerical modeling program included developing finite element models using ABAQUS software to evaluate the effect of geogrid location, thickness of the base course layer, tensile modulus of geogrid reinforcement, and strength of subgrade material on the benefits of geogrid base reinforcement in flexible pavements.

This report will discuss only the results of large-scale in-box and full-scale ALF cyclic plate load tests. The results of small-scale testing and finite element numerical analysis were presented in another report [1].

The large-scale cyclic plate load tests were conducted inside a test box [with dimensions 6.5 ft. \times 6.5 ft. \times 5.5 ft. (1.98 m \times 1.98 m \times 1.68 m)], using a servo-hydraulic actuator, on flexible pavement sections with and without geogrid base reinforcement. A 9-kip load at a frequency of 0.77 Hz was applied through a 12-in. (305-mm) diameter steel plate. The parameters studied in the model tests included the aperture shape (geometry) of geogrid, tensile modulus of geogrid, and the location of geogrid. The tests also included measuring the stress distribution and permanent vertical strain in the subgrade, the excess pore water pressure development in the subgrade, and the strain distribution along the geogrid.

The full-scale testing included both cyclic late load tests and rolling wheel load tests on seven full-scale field pavement sections at the Louisiana Pavement Research Facility (PRF) site. Six types of base materials (including raw BCS, class C fly ash stabilized BCS, 120 grade GGBFS stabilized BCS, FA stabilized RAP, and FA stabilized RAP and soil cement blend) and two types of subbase materials (including lime and cement treated soil) were tested. The performance of different base/subbase materials was compared. The difference in pavement response between cyclic plate and rolling wheel loads was discussed.

METHODOLOGY

In this study, an indoor cyclic plate load testing equipment was developed for the purpose of evaluating the performance of base and subgrade soils in flexible pavement sections under repeated loading test conditions. The testing equipment was used to conduct an in-box large-scale testing program to evaluate the performance and benefits of geogrid base reinforcement for application to flexible pavements. The cyclic plate load testing equipment was also used to test the full-scale test lane sections built at the PRF site to evaluate the performance of pavement sections with different base/subbase materials. The pavement response from cyclic plate load tests was compared with the results of rolling wheel accelerated load testing.

Development of an Indoor Cyclic Plate Load Test

A test box was constructed having inside dimensions of 6.5 ft. (1.98 m) (length) \times 6.5 ft. (1.98 m) (width) \times 5.5 ft. (1.68 m) (height). The side and back walls consisted of 1-in. (25.4-mm) thick steel, which were braced with stiffeners to avoid lateral yielding during construction and loading of test sections. Detachable channel steel beams were used for the front wall to facilitate the construction of test sections. They were attached to the test box using bolt and nut assemblies. Two I beams were fixed on the top side of the walls to serve as the support base for the crosshead. The crosshead consists of another two I beams that allowed to move along the two base I beams. A hydraulic actuator, which has a force rating of 22 kips (100 kN) and a dynamic stroke of 6 in. (152.4 mm), was attached between the two I beams of the crosshead. The crosshead was bolted to the support base I beams while the test was running. The cyclic load was applied through a steel rod that fits into a concave-shaped hole on the loading plate that sat on the surface of the test section. A FlexTest GT test controller connected to a desktop computer controlled the load-time history applied to the plate. Figure 1 shows a schematic of the indoor cyclic plate load test equipment. Figure 2 shows an actual photo of the indoor test equipment.

The hydraulic actuator with the crosshead can be detached from the box and moved to the field for in-situ testing. A field frame consisting of two I beams was constructed to support the crosshead. Six steel blocks were placed on the top of the crosshead to serve as the deadweight supports during the test. Figure 3 shows a schematic of the field cyclic plate load test equipment. Figure 4 shows an actual photo of the field test equipment.

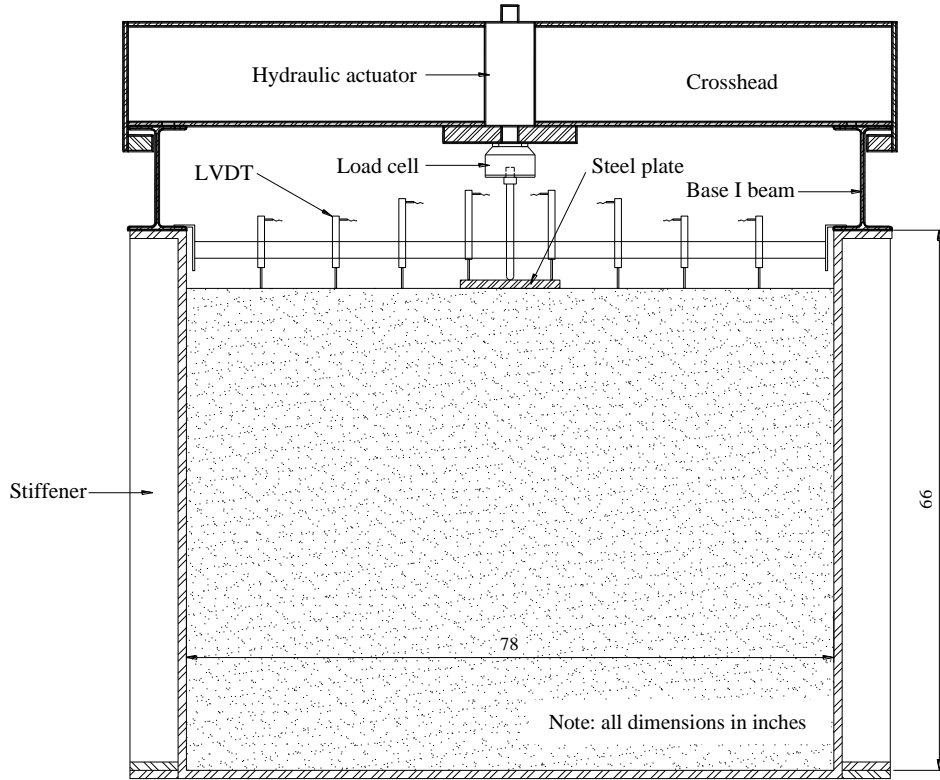


Figure 1
Schematic of the indoor cyclic plate load test equipment



Figure 2
Image of the indoor cyclic plate load test equipment

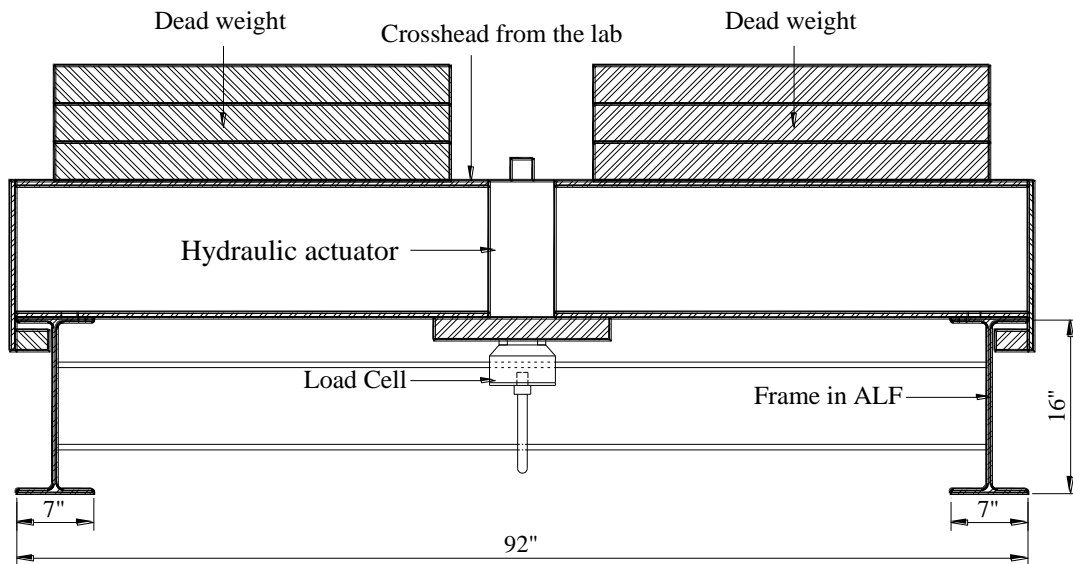


Figure 3
Schematic of the field cyclic plate load test equipment



Figure 4
Image of the field cyclic plate load test equipment

The new in-box actuator testing equipment can be used for testing pavement sections of different base materials, different subgrade conditions, different cross sections, and different loading conditions. In addition, the equipment can be used for other pavement and

geotechnical applications such as testing new materials/products, new stabilizing techniques, and new design methodologies. In this study, the cyclic plate load testing equipment was used in the box to evaluate the performance and benefits of geogrid base reinforcement in flexible pavements; and to evaluate and compare the performance of several full-scale test lane sections, built at PRF site, with the rolling wheel accelerated load testing.

Laboratory Cyclic Plate Load Tests

Laboratory in-box cyclic plate load tests were conducted to investigate the potential benefits of using geogrid base reinforcement in flexible pavements, including the influence of various parameters on the performance of geogrid base reinforcement. The experimental study also included the investigation of the stress distribution and permanent vertical strain in the subgrade, the excess pore water pressure development in the subgrade, and the strain distribution along the geogrid.

Test Equipment

The indoor cyclic plate load testing equipment, described earlier, was used in this study. Figure 5 presents the photo of the indoor test section. A cyclic load was applied through a steel rod that fits into a concave-shaped hole on the loading plate that sits on the surface of the hot mix asphalt (HMA) layer. The loading plate was a 1-in. (25.4-mm) thick steel plate and 12-in. (305-mm) diameter. A 0.0762-in. (3-mm) thick rubber was attached to the bottom of plate to insure proper seating. The maximum applied load in the tests was 9,000 lb. (40 kN), which results in a loading pressure of 80 psi (550 kPa) that simulates dual wheels under an equivalent 18,000 lb. (80 kN) single-axle load. The load pulse, as shown in Figure 6, consists of a linear load increase from 500 lb. (2.2 kN) to 9,000 lb. (40 kN) in 0.3 second, followed by a 0.2-second period where the load is held constant at 9,000 lb. (40 kN), followed by a linear load decrease to 500 lb. (2.22 kN) over a 0.3-second period, then followed by a 0.5-second period of 500 lb. (2.22 kN) before the next loading cycle starts. This load pulse results in a frequency of 0.77 Hz.

Pavement Layer Materials

HMA Concrete. The HMA mix used in the construction of the pavement test sections was a 0.75 in. (19.0 mm) design level 2 [i.e., 3-30 million equivalent single axis loads (ESALS)] superpave mixture currently in use in the state of Louisiana [35]. The optimum asphalt binder [classified as PG 76-22M according to the Performance Grade (PG) specification] content was 4.1 percent. The theoretical maximum specific gravity of the HMA was 2.51. The dust to binder ratio was 1.18.

Base Course Material. Kentucky crushed limestone was used in the base course layer for all test sections. The crushed limestone had a 100 percent passing 1.5-in. (38.1-mm) opening sieve; 92 percent passing 0.75-in. (19-mm) opening sieve; 61 percent passing No. 4 opening sieve; and 0.35 percent passing No. 200 opening sieve. The corresponding effective particle size (D_{10}) = 0.015 in. (0.382 mm), the D_{15} = 0.022 in. (0.551 mm), the mean particle size (D_{50}) = 0.123 in. (3.126 mm), the uniformity coefficient (C_u) = 11.80, and the coefficient of curvature (C_c) = 1.07. The maximum dry density, as determined by the Standard Proctor test in accordance with ASTM D698, is 140 lb/ft³ (2,247 kg/m³) at an optimum moisture content of 6.6 percent. This crushed limestone is classified as GW and A-1-a according to the Unified Soil Classification System (USCS) and the American Association of State Highway and Transportation Officials (AASHTO) classification system, respectively.

Subgrade. The subgrade soil consisted of a silty clay, having a liquid limit (LL) of 31, a plasticity index (PI) of 15, a mean particle size (D_{50}) of 0.00095 in. (0.024 mm), and a D_{85} of 0.0033 in. (0.085 mm). This soil had 72 percent silt and 19 percent clay. The maximum dry density of the soil is 104 lb/ft³ (1,670 kg/m³), with an optimum moisture content of 18.75%, as determined by the Standard Proctor test. The silty clay soil was classified as CL according to the USCS and A-6 according to the AASHTO classification system.

Geogrid. Four different geogrids, GG1, GG2, GG3, and GG4, were used to reinforce the base course layer in the test sections. These geogrids have a punched structure and are made from polypropylene with different geometries. The physical and mechanical properties of these geogrids, as provided by the manufacturers, are listed in Table 1.

Table 1
Properties of geogrids

Reinforcement	Aperture Shape	T ^a , lb/ft		J ^b , lb/ft		Aperture Stability kg-cm/deg	Aperture Size, in.
		MD ^c	CD ^d	MD ^c	CD ^d		
GG1 biaxial geogrid		280	450	14,000	22,500	3.2	1.0 × 1.3
GG2 biaxial geogrid		410	620	20,500	31,000	6.5	1.0 × 1.3
GG3 triaxial geogrid		590 ^e		29,500 ^e		3.6	1.6 × 1.6 × 1.6
GG4 triaxial geogrid		650 ^e		32,500 ^e		7.8	1.6 × 1.6 × 1.6

^aTensile Strength (at 2% strain) (in accordance with ASTM D6637 for GG1 and ISO 10319:1996 for GG2), ^bTensile Modulus (at 2% strain), ^cMachine Direction, ^dCross Machine Direction, ^eRadial Direction



Figure 5
Laboratory test box, hydraulic actuator, and reaction system

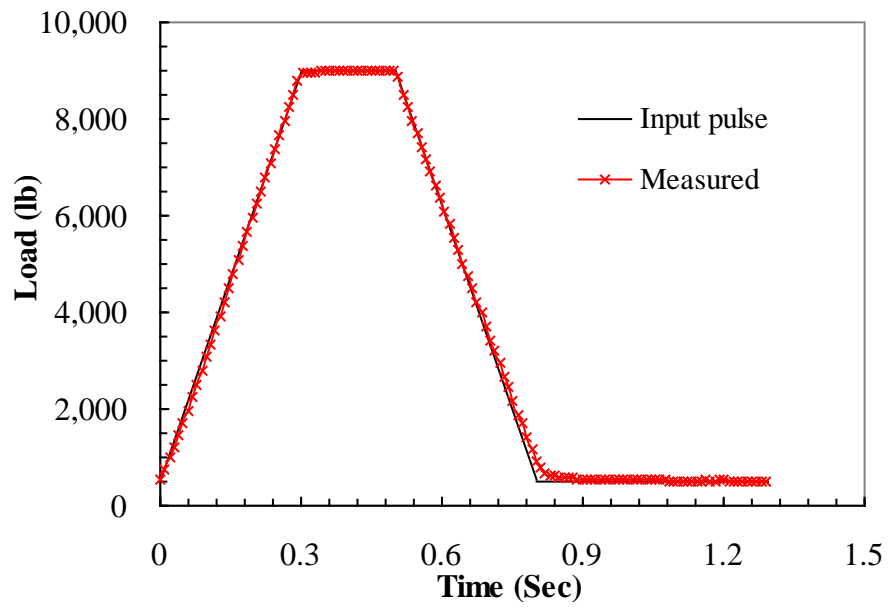


Figure 6
Load pulse applied in the test

Testing Program and Sample Preparation Techniques

The silty clay subgrade was first placed and compacted in lifts inside a steel box. The thickness of each lift was 6 in. (152.4 mm). The target dry density and water content of the subgrade were 100 lb/ft³ (15.7 kN/m³) and 22 percent, respectively, to achieve a weak subgrade of CBR = 0.5 percent. One unreinforced section that was compacted at an optimum moisture content (CBR = 8 percent) was also prepared to compare the performance difference between a weak and a strong subgrade. The subgrade was prepared by using a tiller to mix the silty clay and water. Then, the silty clay was raked level and compacted using an 8-in. × 8-in. (203.2-mm × 203.2-mm) plate adapted to a vibratory Bosch Brute model 11304 breaker hammer to the predetermined height to achieve the desired density.

After the completion of subgrade preparation, the instrumentations and the geogrid were installed. When installing the soil strain gage, a round hole was excavated to the predetermined depth with a hand trowel. The linear variable displacement transducer (LVDT) was placed vertically into the hole (Figure 7). The silty clay was backfilled and compacted with a screwdriver handle around the LVDT.

To install the piezometers, short trenches were first excavated to the predetermined depth with a hand trowel (Figure 8). Horizontal holes with a slightly larger diameter than the piezometer were excavated at the end of each trench. The ready-saturated piezometers were then inserted into the holes and covered immediately with a saturated silty clay soil.

When installing pressure cells, holes with the same shape but slightly larger than the pressure cells were excavated to the predetermined depth with a hand trowel. The bottom of each hole was flattened with a steel plate gently hit by the compaction hammer. The pressure cells were then placed into the holes and adjusted until leveled with the assistance of a small bubble level placed on the pressure cell (Figure 9). The silty clay was backfilled and compacted over the pressure cells. The amount of clay needed in backfilling an excavation was estimated by removing the amount of clay occupied by the pressure cell, which was calculated by multiplying the density of clay by the approximate volume of the pressure cell from the excavated clay. To minimize an over-registration/under-registration of pressure due to possible over-compaction/under-compaction, a tight control of the backfill compaction was made to ensure that the density of the backfill was close to that of the surrounding soil.

After installation of pressure cells and piezometers, the geogrid with strain gages was placed on top of the subgrade layer (Figure 10). To protect the strain gages from damage during the compaction of base course layer, the gages were covered with a small amount of silty clay

soil and gently compacted by hand before the base course material was spread over the geogrid layer.

After the installation of the geogrid, the base course layer was prepared by placing the crushed limestone in 6-in. (152.4-mm) thick lifts, mixing with the desired water content, and then compacting to the predetermined height. The target dry density and water content of the base course layer were 138 lb/ft³ (21.66 kN/m³) (i.e., 98 percent degree of standard proctor compaction) and 6.0 percent, respectively.

The surface asphalt concrete (AC) layer was consequently prepared by placing prime coat on the top of the base layer, followed by placing cold-mix asphalt concrete along the sides of the box with a width of 12 in. (305 mm) (Figure 11). The remaining center area of the test box [54 in. (1371.6 mm) wide square) was left for the HMA. The cold mix asphalt at the boundary area between the two mixes was covered with the tack coat. The HMA was obtained from a local asphalt plant. It was placed in the oven to age for about 4 hours at a temperature of 300°F (150°C). Once the mixture reached the proper compaction temperature [i.e., 300°F (150°C)], it was spread over the reserved central area in the test box, raked level, and immediately compacted to the predetermined height using the Bosch Brute breaker hammer.



Figure 7
Placement of soil strain gauge



Figure 8
Placement of piezometers



Figure 9
Placement of pressure cells



Figure 10
Placement of geogrids with strain gages



Figure 11
Preparation of the AC layer

The nuclear density gauge, Geogauge (GG), and Vane Shear Testing Apparatus were deployed to measure the in-place properties of the subgrade layer. The nuclear density gauge, GG, light falling weight deflectometer (LWD), and dynamic cone penetrometer (DCP) were

deployed to measure the in-place properties of the base course layer. The GG, LFWD, and Portable Seismic Pavement Analyzer (PSPA) were deployed to measure the in-place properties of the HMA layer. At least five measurements were performed for each property.

Figure 12 depicts a typical flexible pavement section with geogrid base reinforcement, which describes the geometric parameters and a typical layout of the instrumentations used in the present study.

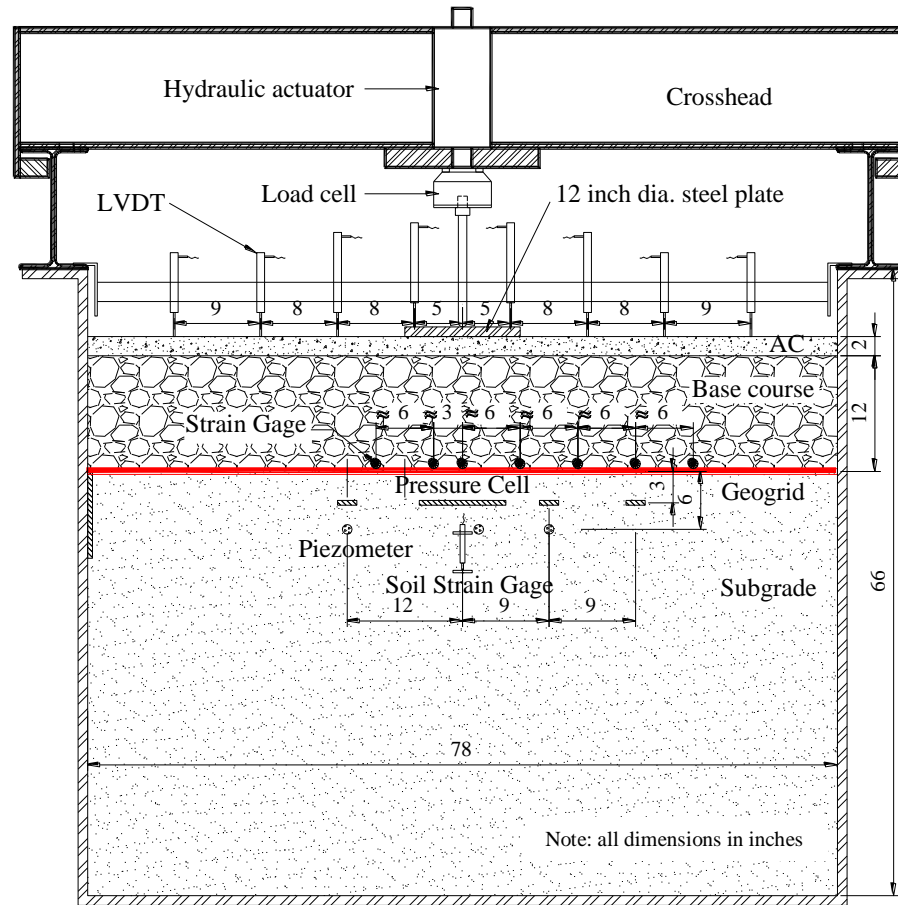


Figure 12
Schematic of the indoor test box for cyclic load testing

Instrumentation Program

Instrumentation. A load cell (MTS Series 661 Force Transducer), which was used to measure the applied load, was attached to the piston rod emerging from the actuator. The load cell has a measurement range of 0-22 kips (0-100 kN). A central LVDT, which was coaxially mounted within the actuator piston rod, provided measurement of the piston rod displacement.

Another eight LVDTs from RDP Electronics were used to monitor the surface deformation of the HMA layer. The raw output reading of the LVDTs is in voltage (v). The LVDTs, which were mounted on a steel reference beam, were installed on both sides of the actuator in a straight line as shown in Figure 12. Four LVDTs (DCTH1000A) that have a reading range of ± 1 in. (25.4 mm) were placed closer to the center of the loading plate, with the two closest ones sat on the loading plate. The other four LVDTs (DCTH500A) with a reading range of ± 0.5 in. (12.7 mm) were placed relatively far away from the center of the loading plate.

The pore water pressures were measured using Model 4500AL VW piezometers from Geokon, Inc., which were installed within the subgrade soil at specified locations/depths as shown in Figure 12. This type of transducer allows for the measurement of positive pore pressures up to 25 psi (172 kPa) and negative pore pressures up to 1 Bar (100 kPa). The vibrating wiring sensor is slow in response and may not be suitable for the measurement of rapidly changing pressures. The very immediate response of pore water pressure to the applied load in this study may not be captured fully by the VW piezometer. Nevertheless, the VW piezometer can give a good trend in the development of pore water pressure with cyclic loading as the dissipation of pore water pressure is slow in clayey soil, as will be shown later in this report.

The vertical soil strain in the subgrade beneath the center of the loading plate was measured using a soil strain gage, which is an LVDT fitted with two 2-in. \times 0.6-in. \times 0.2-in. (50.8-mm \times 15.2-mm \times 5.08-mm) steel plates. The LVDT used was RDP model D5/400W. The gage length was set as 4 in (101.6 mm).

The stress distribution in the subgrade was measured using type 0234 pressure cells from Kulite and Model 3500-1 earth pressure cells from Geokon, Inc. The pressure cells were installed within the subgrade at specified locations/depths as shown Figure 12. An initial attempt to use Kulite LQ-080U soil stress gage type was not satisfactory because of its small size and easy to rotate during compaction, which convinced the authors to switch to Kulite type 0234 pressure cells.

The Kulite type 0234 pressure cell, which utilizes a solid state silicon pressure transducer as the basic sensing element, is a 2.2 in. (55 mm) in diameter with a thickness of 0.7 in. (18.3 mm). The Geokon 3500 earth pressure cell, which utilizes a semiconductor pressure transducer as its basic sensing element, has a diameter of 9 in. (229 mm) and a thickness of 0.24 in. (6 mm). The Geokon 3500 pressure cell consists of two circular stainless steel plates separated by a narrow space filled with deaired hydraulic oil. The earth pressure felt by the cell squeezes the two plates together, thus building up the hydraulic oil pressure, which is

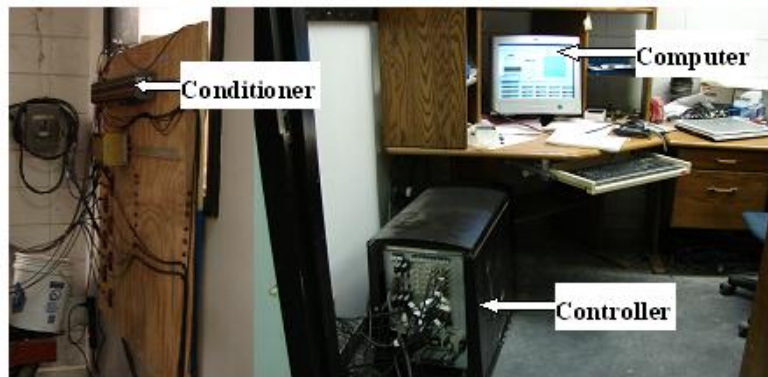
then transmitted to the pressure transducer mounted several centimeters away from the cell. One of the advantages of the Geokon pressure cell is its high aspect ratio (diameter: thickness) d/t of 38, which is much higher than that of the Kulite type 0234 pressure cell (d/t of 3). A thin cell usually alters the stress field in the soil less than a thick cell. However, since the Geokon 3500 pressure cell has a larger diameter, the measured stress represents an average value over a larger area, so it is not accurate for point stress measurement. As described earlier, for the Geokon 3500 pressure cell, the earth pressure is converted to hydraulic oil pressure and then transmitted to the pressure transducer. As such, the response time of the Geokon 3500 pressure cell is longer than that of the Kulite 0234 type pressure cell.

The strain distribution along the geogrid was measured using electrical resistance strain gages from Vishay Micro-Measurements that were placed at different locations along the geogrid as shown in Figure 12. The raw outputs of strain gages are in millivolts (mv). Under cyclic loading, the geogrid is expected to experience both cyclic elastic strain and accumulation of permanent (plastic) strain. This requires the foil strain gage to have both a relatively high elongation capability and a good fatigue life. However, these two requirements are contradictory, and an optimization of the strain gage properties is desirable. Because of previous success in static application, EP-08-250BG-120 strain gages were chosen in this study as an initial attempt of strain measurements. This strain gage is made of annealed constantan alloy, which is very ductile but has very high elongation ability. The strain gages have a resistance of $120 \pm 0.5\% \Omega$ and a strain range of $\pm 20\%$, but only $\pm 7.7859\%$ of the range was activated. The fatigue life provided by the manufacturer is about 10^3 cycles under dynamic strain level of 0 to $3000\mu\epsilon$, which is determined based on a $500\mu\epsilon$ zero-shift failure criterion [36].

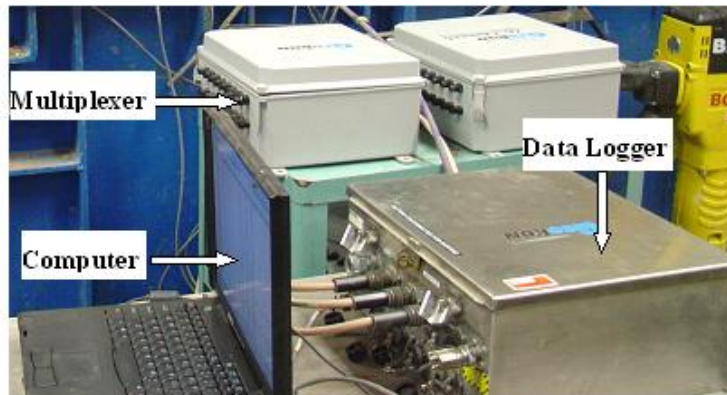
Data Acquisition System. The main data acquisition system, as shown in Figure 13a, consisted of the DSC SGA conditioning module and a FlexTest GT test controller connected to a desktop computer running the Station Manage Software package marketed by the MTS Systems Corporation. The magnitudes of the output signals from the pressure cells and the strain gages were too small to be read by the controller, and the pressure cells and the strain gages were therefore connected to the signal conditioners first. The signal conditioners supplied excitation voltage to the sensors and amplified their output signals (voltage). The initial offset values of the conditioners were zeroed first. The maximum electrical inputs of the conditioners, i.e., the full output signals of sensors, were set to 100 mv for all sensors. The spans of the conditioners were adjusted so that the output signals of conditioners were 100 times the electrical input of the conditioners. The excitation voltages were adjusted to 7.5 VDC for the Kulite type 0234 pressure cells, 10 VDC for the Geokon 3500 pressure cells,

and 2.5 VDC for the strain gages. The LVDTs that contain built-in signal conditioners were connected to a terminal board with a power supply. The power input for the LVDT internal conditioners was 15 VDC dual power supplied by a linear regulated power supply with AC-DC dual tracking outputs. The electrical output of the LVDTs was ± 5 VDC. The output signals (voltage) of all the sensors were sent through the BNC cable to the FlexTest GT test controller, which digitized the output signals of all sensors (voltage). The digitized output signals (binary digit) were sent to the software program. The software then converted the digitized output signals of all sensors to engineering units (psi, $\epsilon\%$, and in.).

A separate acquisition system was used for the VW piezometers because the FlexTest GT test controller cannot read the vibration wire sensors. This data acquisition system, as shown in Figure 13b, consisted of Geokon Model 8032 16/32 channel multiplexers and a Geokon Model 8020 MICRO-10 Datalogger connected to a laptop computer running a Mutilogger Software package marketed by Canary Systems, Inc. The detailed description of this system can be found in Abu-Farsakh et al. [37].



(a) Main data acquisition system



(b) Data acquisition system for piezometer

Figure 13
Data acquisition system

Instrumentation, Preparation and Calibration. A single active strain gage element in a quarter Wheatstone Bridge configuration was used in this study. Three dummy resistors, a matched pair (MR2-350-128), and a precision resistor (S-120-01) to match the strain gage resistance were chosen for bridge completion. Grid surface preparation involved degreasing with isopropyl alcohol, abrading the surface of the rib with a fine grit sand paper in diagonal directions, surface conditioning, and neutralizing followed by bonding the gage to the grid using adhesive resin. The strain gages and lead wires were protected by water-proof silicone rubbers. The strain gages were statically calibrated in the laboratory using the United Mechanical Testing Machine SFM-30E manufactured by the United Calibration Corporation. The test follows the procedure described in the ASTM D6637-01. The measured strain data presented in this study were corrected based on the calibration test results. The corresponding strain correction factors were 1.1 in machine direction and 1.07 in cross-machine direction for GG1 geogrids and 1.07 for GG2 geogrids. More details of calibration of strain gages are available in Abu-Farsakh et al. [37].

All other sensors were calibrated by the manufacturers before shipment to the laboratory. However, before the sensors were installed, they were checked again in the laboratory to check if they were functioning properly with the factory calibration factors. The LVDTs were calibrated by comparing the electrical outputs of the LVDTs and the readings of a micrometer. To provide an optimum calibration, the method of least squares was used to fit a series of data pairs. Plotting these data also allows us to check the LVDTs for any possible non-linearity.

The pressure cells were calibrated by simply placing increments of known dead weight on the cells before each installation. The applied pressures and the measured pressures were compared to verify the calibration factors provided by the manufacturer. The method of least squares was then used to fit the data pairs.

The piezometers were calibrated by simply placing them at the bottom of a container and measuring the height of water in increments. The applied and measured water pressures were compared to verify the factory calibration factors. Although the calibration techniques for the pressure cells and piezometers may not be very accurate, it is simple and gave the authors confidence that the measured stresses and pore water pressures were accurate. Each piezometer was deaired by inserting it in a water-filled tube with the gap sealed with grease and then applying a vacuum until no bubbles were visually observed. The piezometers were kept in deaired water to maintain saturation condition until installation.

Field Cyclic Plate Load and Rolling Wheel Load Tests

Two series of tests, cyclic plate load tests and rolling wheel load tests, were conducted to investigate the field performance of raw BCS, stabilized BCS, stabilized RAP, and stabilized soil as base/subbase materials and to identify the differences in pavement response to cyclic plate and rolling wheel loads.

Test Facilities

Cyclic Plate Load Tests. Cyclic plate loads were applied using an MTS hydraulic actuator, which has a force rating of 22 kips (100 kN) and a dynamic stroke of 6 in. (152.4 mm). Figure 14 presents a photo of the cyclic plate loading test setup. The cyclic load was applied through a steel rod that fits into a concave-shaped hole on the loading plate that sits directly on the surface of the HMA (hot mix asphalt) layer. The loading plate used has a 1-in. (25.4-mm) thick steel plate and a 12 in. (305 mm) diameter. The maximum applied load in all tests was 12,000 lb. (53 kN), which results in a loading pressure of 106 psi (732 kPa) that simulates the dual wheels under an equivalent 18,000 lb. (80 kN) single axle load. The load pulse, as shown in Figure 15, has a linear load increase from 500 lb. (2.2 kN) to 12,000 lb. (53 kN) in 0.3 second, followed by a 0.2-second period where the load is held constant at 12,000 lb. (53 kN), followed by a linear load decrease to 500 lb. (2.2 kN) over a 0.3-second period, then followed by a 0.5-second period of 500 lb. (2.2 kN) (rest period), before the next loading cycle is applied. This load pulse results in a frequency of 0.77 Hz.

Rolling Wheel Load Tests. The rolling wheel loads were applied using an Australia-designed ALF (Accelerated Load Facility) (Figure 16), which simulates half of a single axle with "X" ZE Michelin dual tires. The load is adjustable from 9,750 lb. (43.4 kN) to 18,950 lb. (84.4 kN). The starting load was 9,750 lb. (43.4 kN). The load was increased to 12,050 lb. (53.6 kN) after 175,000 cycles (241,039 ESALs), then to 14,350 lb. (63.8 kN) after 225,000 cycles (401,714 ESALs), and then to 16,650 lb. (74.1 kN) after 325,000 cycles (1,048,019 ESALs). The tire pressure was set to 105 psi (724 kPa). The shape of the applied load was approximated as two 6-in. (152.4-mm) apart uniformly loaded rectangular areas [9 in. (228.6 mm) × 10.7 in. (271.8 mm)], as shown in Figure 16, in this study. With a computer-controlled load trolley, the weight and movement of traffic were simulated in one direction at a speed of 10.5 mph (16.8 km/h). Lateral wander normally distributed over a width of 30 in. (762 mm) 15 in. (381 mm) at each side of the pavement centerline) was considered in this experiment.



Figure 14
Cyclic plate load testing equipment

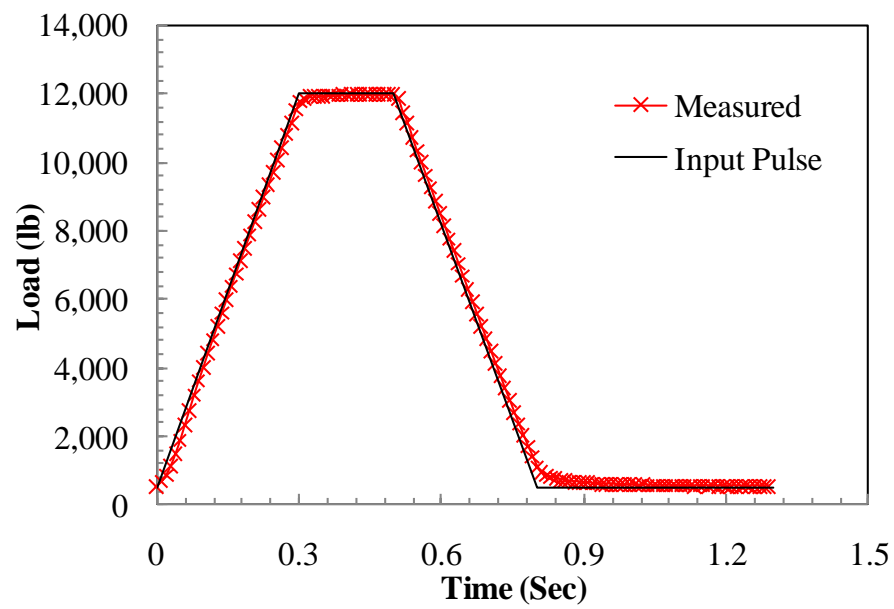


Figure 15
Load pulse applied in the test

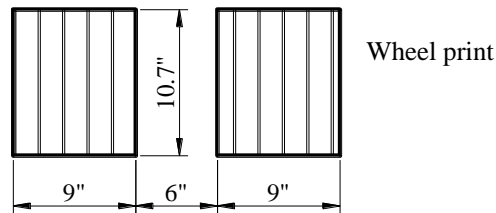


Figure 16
Rolling wheel load testing facility

Pavement Test Sections

Seven pavement testing sections were constructed at the Louisiana Pavement Research Facility (PRF) site (Figure 17) using normal highway construction equipment and procedures. The locations of the cyclic plate load tests and the rolling wheel load tests for each section are shown in Figure 17. All sections consisted of a similar 2-in. (51-mm) HMA top layer, a 8.5-in. (216-mm) base layer, a 12-in. (305-mm) subbase layer, and a similar subgrade layer (Figure 18). Base and subbase materials varied between the different sections. A thin HMA layer was used due to the consideration that the purpose of testing was to investigate the performance of base/subbase materials.

As shown in Table 2, pavement test sections 1, 2, 3, and 4 have the same subbase material, lime treated soil (LTS), with various base course materials: raw BCS, Class C fly ash stabilized BCS, 120 grade GGBFS stabilized BCS, and crushed limestone, respectively. Pavement test sections 5, 6, and 7 have cement treated soil (CTS) subbase material with base course materials of crushed limestone, FA stabilized RAP, and FA stabilized RAP and soil cement blend, respectively.

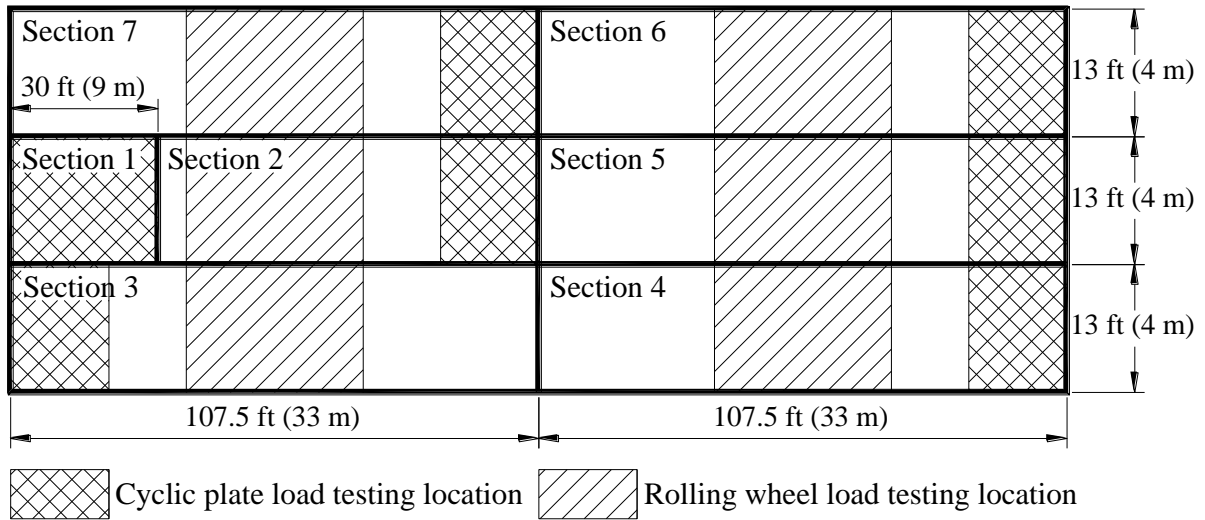


Figure 17
Plan layout of testing sections (not to scale)

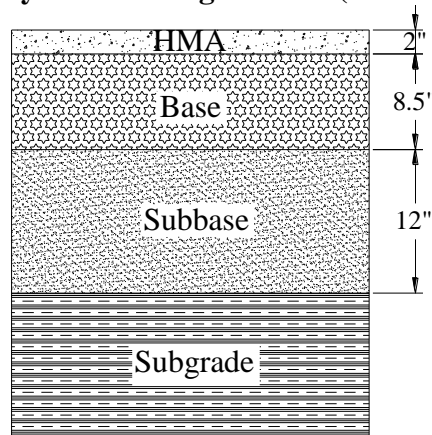


Figure 18
Pavement structure of testing sections (not to scale)

Table 2
Combination of base/subbase materials in pavement test sections

Section	Base	Subbase	Rolling wheel load		Cyclic plate load	
			Test Start	Test End	Test Start	Test End
1	BCS+LTS	Raw BCS	N/A	N/A	11/2008	12/2008
2	BCS/Flyash+LTS	Lime (10% by volume) stabilized BCS treated soil	10/2005	10/2006	12/2008	01/2009
3	BCS/Slag+LTS		10/2005	10/2006	10/2008	11/2008
4	LS+LTS		01/2007	04/2007	05/2008	06/2008
5	LS+CTS	Cement (8% by volume) treated soil	01/2007	08/2007	06/2008	07/2008
6	100%RAP/FA+CTS		01/2007	07/2007	08/2008	09/2008
7	50%RAP50%SC/FA + CTS		10/2005	06/2006	01/2009	02/2009

Pavement Layer Materials

Hot Mix Asphalt (HMA) Concrete. A 19-mm Superpave mixture, designed for intermediate volume roads (3-30 million ESALs) in Louisiana, was used as the surface layer in all test sections. The mixture contained 14.3% RAP materials. The optimum asphalt binder content was 4.4%, including 3.7% PG76-22 virgin binder and 0.7% recycled binder (from the RAP). Laboratory results for HMA cores, which were taken at the time when the rolling wheel load tests were performed and at the time when the cyclic plate tests were performed, indicated similar resilient modulus of about 450 ksi (3100 MPa) at the room temperature.

Base Course Materials. Six types of base materials were tested. Raw BCS base was designed for section 1. Two different types of stabilization agents were added to improve the water resistance of BCS. One is 10% Grade-120 ground granulated blast furnace slag by volume (section 2); and the other is 15% Class C fly ash by volume (section 3). The base course material used for sections 4 and 5 was Kentucky crushed limestone. The foamed asphalt stabilized bases were designed for sections 6 and 7, according to the standard *Wirtgen Cold Recycling Manual*. The mixture for section 6 consisted of 97.5% RAP and 2.5% PG58-22 binder; while the mixture for section 7 consisted of 48.6% RAP, 48.6% recycled soil cement and 2.8% PG58-22 asphalt binder. The designed air voids for sections 6 and 7 were 15.3% and 20.3%, respectively. The RAP had a 100% passing 0.75 in. (19 mm) opening sieve, a 97% passing 0.5 in. (12.7 mm) opening sieve, a 65% passing No. 4 opening sieve, and a 9% passing No. 200 opening sieve with an asphalt content of 4.8%. The physical and mechanical properties of the base course materials determined from the laboratory tests are summarized in Table 3 [33 and 38].

Subbase and Subgrade Material. A silty-clay embankment soil, having a liquid limit of 31 and a plastic index (PI) of 12, was used as the subgrade soil. This soil contains 60.3% silt and 23.5% clay. The top 12 in. (305 mm) of the subgrade was treated with lime or cement to provide a subbase layer of low plasticity and low water susceptibility. For lime treated soil (LTS) sections (sections 1, 2, 3, and 4), 10% lime was added to the top 12 in. (305 mm) of the subgrade soil by volume. For CTS sections (sections 5, 6, and 7), 8% cement was added to the top 12 inch (305 mm) of the subgrade soil by volume. The physical and mechanical properties of untreated and lime/cement treated subgrade soils are summarized in Table 4 [38].

Table 3
Properties of base materials

		BCS	BCS /Fly ash	BCS /Slag	Crushed Limestone	100% RAP/FA	50%RAP 50%SC/FA
UCS (psi) ¹		54.5 ²	60.5 ² (65.8 ³)	672.7 ² (5.0 ³)	N/A	N/A	N/A
M _r (psi) ⁴		80,061	89,923	105,196	40,030	30,023	32,924
ε _p (%) ⁵		0.1191	0.0155	0.0048	0.2734	2.1101	0.5057
Sieve size (in.)	Sieve size (mm)	Gradation (% passing)					
2	50	100	100	100	100	100	100
1.5	37.5	98	98	98	100	100	100
1	25	95	95	95	97	100	100
3/4	19	91	90	91	88	94	95
1/2	12.5	85	83	76	74	79	83
3/8	9.5	81	79	69	67	66	72
# 4	4.75	71	71	54	50	43	52
# 8	2.36	63	64	41	36	29	38
# 16	1.18	60	61	35	26	19	29
# 30	0.6	59	59	31	20	11	21
# 50	0.3	57	57	29	15	5	15
# 200	0.075	56	54	27	11	3	10
Optimum moisture content		11.3	12.5	11.5	6.3	7.5	10.0
Maximum dry unit weight (lb/ft ³)		110	119.7	110.1	150.9	126	118.4
USCS ⁶		N/A	N/A	N/A	GM	GP	GM
AASHTO		N/A	N/A	N/A	A-1-a	A-1-a	A-1-a

¹UCS: unconfined compressive strength ²unsoaked after 28 days of curing in the lab; ³soaked after 28 days of curing in the lab; ⁴resilient modulus after 28 days of curing in the lab ($\sigma_d = 15$ psi (103.4 kPa), $\sigma_c = 5$ psi (34.5 kPa)); ⁵permanent deformation after 28 days of curing in the lab ($\sigma_d = 15$ psi (103.4 kPa), $\sigma_c = 5$ psi (34.5 kPa), N = 10,000); ⁶USCS: Unified Soil Classification System.

Table 4
Properties of subbase and subgrade materials

	Subgrade	Lime treated soil subbase	Cement treated soil subbase
UCS (psi) ¹	N/A	N/A	233.5
M _r (psi) ²	5,656	20,595	62,366
ε _p (%) ³	0.283	0.0071	0.0043
Optimum moisture content	18.5	N/A	N/A
Maximum dry unit weight (lb/ft ³)	108.9	N/A	N/A
Liquid limit	31	N/A	N/A
Plastic index	12	N/A	N/A
USCS	CL	N/A	N/A
AASHTO	A-6	N/A	N/A

¹after 7 days of curing in the lab; ²resilient modulus after 28 days of curing in the lab ($\sigma_d = 6$ psi (41.4 kPa), $\sigma_c = 2$ psi (13.8 kPa)); ³permanent deformation after 28 days of curing in the lab ($\sigma_d = 6$ psi (41.4 kPa), $\sigma_c = 2$ psi (13.8 kPa), N = 10,000).

DISCUSSION OF RESULTS

Evaluation of Geogrid Base Reinforcement Using Cyclic Plate Load Testing

Test Results

In-Place Properties. The mean, minimum, and maximum values of the in-place properties of the subgrade, base course, and HMA materials are summarized in Table 5, Table 6, and Table 7, respectively, for all test pavement sections. The corresponding coefficients of variation (CV) are also presented in the tables. The air voids, density, and resilient modulus of the HMA were obtained from the core samples taken after the tests.

Cyclic Plate Load Tests. A total of 10 tests were conducted on different pavement sections: one unreinforced section on strong subgrade (CBR = 8%), two unreinforced sections on weak subgrade (CBR = 0.5%), four reinforced sections on weak subgrade with one geogrid layer placed at the base/subgrade interface, two reinforced sections on weak subgrade with one geogrid layer placed at the middle of the base layer, and one reinforced section on weak subgrade with one geogrid layer placed at the upper one third of the base layer. The traffic benefit ratio (TBR) was used to evaluate the benefit of geogrid base reinforcement. The TBR is defined as the number of load cycles carried by the reinforced section at a specific rut depth divided by that of an equivalent unreinforced section. The results of the tests for unreinforced and reinforced pavement sections are summarized in Table 8. The results of the accelerated load tests are graphically presented in Figure 19 for different types of geogrid placed at interface. Figure 20 presents the test results for GG3 and GG4 geogrids placed at different locations. Figure 21 shows the results of GG4 geogrid placed at the middle of the base layer with/without the application of prime coat. The comparison between the unreinforced weak subgrade sections, the unreinforced strong subgrade section and the GG4 reinforced section is depicted in Figure 22.

Table 5
In-place properties of subgrade

Test Section		MC ¹ %	DD ² pcf (kg/m ³)	E _{GG} ³ ksi (MPa)	Shear Strength psi (kPa) ⁴
Unreinforced-1 CBR=0.5%	Mean	21.7	100 (1602)	1.29 (8.9)	N/A
	Min	21.5	98.1 (1571)	1.07 (7.4)	N/A
	Max	21.8	100.8 (1615)	1.51 (10.4)	N/A
	CV(%)	0.8	1.3	18.7	N/A
Unreinforced-2 CBR=0.5%	Mean	22.1	101.3 (1623)	1.20 (8.3)	N/A
	Min	21.4	99.3 (1591)	0.96 (6.6)	N/A
	Max	22.5	102.8 (1647)	1.54 (10.6)	N/A
	CV(%)	2.2	1.4	20.0	N/A
Unreinforced CBR=8%	Mean	18.7	104.1 (1668)	2.78 (19.2)	N/A
	Min	18.1	103 (1650)	2.29 (15.8)	N/A
	Max	19.5	106.2 (1701)	3.28 (22.6)	N/A
	CV(%)	3.1	1.8	17.7	N/A
GG1 at interface CBR=0.5%	Mean	21.6	101.1 (1620)	1.15 (7.9)	0.32 (2.17)
	Min	21.2	98.4 (1576)	1.02 (7.0)	0.26 (1.76)
	Max	21.8	102.8 (1647)	1.23 (8.5)	0.34 (2.35)
	CV(%)	1	1.9	7.9	12.1
GG2 at interface CBR=0.5%	Mean	21.5	101 (1618)	1.16 (8.0)	N/A
	Min	20.5	99.9 (1600)	0.96 (6.6)	N/A
	Max	22.3	101.6 (1627)	1.33 (9.2)	N/A
	CV(%)	3.2	0.6	16.5	N/A
GG3 at interface CBR=0.5%	Mean	21.8	100.7 (1613)	1.20 (8.3)	0.31 (2.14)
	Min	20.8	100 (1602)	0.94 (6.5)	0.30 (2.06)
	Max	22.5	101.6 (1627)	1.39 (9.6)	0.34 (2.35)
	CV(%)	3.5	0.6	14.9	6.5
GG4 at interface CBR=0.5%	Mean	22.3	101.4 (1624)	0.92 (6.4)	0.30 (2.06)
	Min	21.2	100.1 (1603)	0.72 (4.9)	0.27 (1.88)
	Max	23.5	102.7 (1645)	1.30 (9.0)	0.32 (2.23)
	CV(%)	4.9	1.2	24.4	7.3
GG3 at the middle CBR=0.5%	Mean	22.1	102 (1634)	1.13 (7.8)	0.39 (2.67)
	Min	21.1	100.8 (1615)	0.77 (5.3)	0.34 (2.35)
	Max	23.6	102.9 (1648)	1.55 (10.7)	0.43 (3.00)
	CV(%)	3.3	0.9	28	8.9
GG4 at the middle CBR=0.5%	Mean	21.6	101 (1618)	0.90 (6.2)	0.32 (2.21)
	Min	20.6	99.1 (1587)	0.78 (5.4)	0.29 (2.00)
	Max	22.5	102 (1634)	1.16 (8.0)	0.36 (2.47)
	CV(%)	3.3	1.1	19.9	8.1
GG4 at the upper one third CBR=0.5%	Mean	22.3	101.9 (1632)	1.28 (8.8)	0.40 (2.74)
	Min	20.9	100.8 (1615)	1.06 (7.3)	0.37 (2.53)
	Max	23.2	102.9 (1648)	1.57 (10.8)	0.43 (3.00)
	CV(%)	0.9	0.8	16	6.5
GG4 at the middle with prime coat CBR=0.5%	Mean	22.7	102.2 (1637)	N/A	0.41 (2.83)
	Min	22.0	100.9 (1616)	N/A	0.37 (2.58)
	Max	23.4	103.7 (1661)	N/A	0.45 (3.11)
	CV(%)	2.4	1.2	N/A	7.2

¹Moisture content; ²Dry density; ³ $E_{GG} = P(1 - \nu^2) / 1.77R\delta$, P= the applied force, ν =Poisson's ratio, R=outside radius of the Geogauge ring foot, δ =the displacement; ⁴In-situ vane shear test.

Table 6
In-place properties of base course

Test Section		MC ¹ %	DD ² pcf (kg/m ³)	E _{GG} ³ ksi (MPa)	E _{LFWD} ⁴ ksi (MPa)	DCPI mm/blow (CBR) ⁵
Unreinforced-1 CBR=0.5%	Mean	6.1	135.0 (2162)	22.8 (157.5)	3.19 (22.0)	13.2 (16)
	Min	N/A	134.0 (2146)	20.6 (141.8)	2.03 (14)	10.2 (22)
	Max	N/A	136.3 (2183)	24.8 (170.7)	4.35 (30)	16.2 (12)
	CV(%)	N/A	0.8	12.8	25.9	18.8
Unreinforced-2 CBR=0.5%	Mean	6.6	138.1 (2212)	24.3 (167.6)	3.23 (22.3)	9.5 (23)
	Min	N/A	133.4 (2137)	17.9 (123.1)	2.61 (18)	7.6 (30)
	Max	N/A	141.0 (2259)	28.6 (197.4)	4.06 (28)	12.1 (18)
	CV(%)	N/A	2.4	16.7	14.7	24.8
Unreinforced CBR=8%	Mean	6.3	136.2 (2182)	23.1 (159.6)	3.54 (24.4)	10.3 (21)
	Min	N/A	133.4 (2137)	22.2 (153.1)	2.90 (20)	9.9 (22)
	Max	N/A	138.7 (2222)	24.1 (166.2)	4.50 (31)	10.6 (21)
	CV(%)	N/A	2	4.1	15.2	3.1
GG1 at interface CBR=0.5%	Mean	6.0	139.2 (2230)	17.7 (122.2)	3.83 (26.4)	9.1 (25)
	Min	N/A	137.1 (2196)	12.8 (88.0)	3.05 (21)	7.9 (29)
	Max	N/A	140.8 (2255)	23.5 (162.0)	4.79 (33)	10.0 (22)
	CV(%)	N/A	1.0	31	13.9	11.2
GG2 at interface CBR=0.5%	Mean	6.1	136.9 (2193)	N/A	3.16 (21.8)	10.4 (21)
	Min	N/A	133.8 (2143)	N/A	2.90 (20)	8.5 (27)
	Max	N/A	139.9 (2241)	N/A	3.77 (26)	13.6 (16)
	CV(%)	N/A	2.1	N/A	7.2	20.3
GG3 at interface CBR=0.5%	Mean	6.4	138.8 (2223)	24.5 (168.7)	4.47 (30.8)	9.2 (24)
	Min	N/A	137.6 (2204)	20.0 (138.1)	3.63 (25)	7.9 (29)
	Max	N/A	140.3 (2247)	28.4 (195.8)	5.37 (37)	9.9 (22)
	CV(%)	N/A	1.0	14.9	10.6	10.1
GG4 at interface CBR=0.5%	Mean	6.1	141.4 (2265)	25.7 (177.2)	3.81 (26.3)	10.0 (22)
	Min	N/A	138.4 (2217)	19.6 (134.8)	2.90 (20)	8.7 (26)
	Max	N/A	144.7 (2318)	33.9 (234.0)	4.50 (31)	11.6 (19)
	CV(%)	N/A	1.8	24.1	9.0	13.1
GG3 at the middle CBR=0.5%	Mean	5.9	137.9 (2209)	20.5 (141.5)	4.12 (28.4)	9.3 (24)
	Min	N/A	135.1 (2164)	16.7 (114.9)	3.63 (25)	8.5 (27)
	Max	N/A	140.8 (2255)	28.7 (197.8)	4.50 (31)	11.1 (20)
	CV(%)	N/A	2.1	24	6.6	10.8
GG4 at the middle CBR=0.5%	Mean	6.5	139.4 (2233)	24.7 (170.1)	3.95 (27.2)	8.9 (25)
	Min	N/A	136.2 (2182)	19.4 (134.1)	3.48 (24)	8.3 (27)
	Max	N/A	141.9 (2273)	29.3 (201.7)	4.35 (30)	9.2 (24)
	CV(%)	N/A	2.1	15.4	6.6	23
GG4 at the upper one third CBR=0.5%	Mean	6.4	141.5 (2267)	17.7 (122.0)	4.51 (31.1)	9.0 (25)
	Min	N/A	139.7 (2238)	14.5 (100.0)	3.92 (27)	8.4 (27)
	Max	N/A	143.8 (2303)	20.9 (144.0)	5.66 (39)	9.8 (23)
	CV(%)	N/A	1.5	16.1	3.0	8.0
GG4 at the middle with prime coat CBR=0.5%	Mean	6.0	140.3 (2247)	N/A	3.41 (23.5)	N/A
	Min	N/A	137.2 (2198)	N/A	2.90 (20)	N/A
	Max	N/A	143.9 (2305)	N/A	3.92 (27)	N/A
	CV(%)	N/A	1.8	N/A	9.3	N/A

¹Moisture content; ²Dry density; ³ $E_{GG} = P(1-v^2)/1.77R\delta$, P= the applied force, v=Poisson's ratio, R=outside radius of the Geogauge ring foot, δ =the displacement; ⁴ $E_{LFWD} = 2(1-v^2)\sigma R/\delta_c$, σ =the applied stress, R=the loading plate radius of LFWD, δ_c =center deflection of the loading plate; ⁵The number listed in parentheses () is the estimate CBR, = 292/DCPI^{1,12}.

Table 7
In-place properties of HMA

Test Section		E _{GG} ¹ ksi (MPa)	E _{LFWD} ² ksi (MPa)	Density (pcf)	Air Voids (%)	M _r ³ ksi (MPa)	Shear Modulus ⁴ ksi (MPa)
Unreinforced-1 CBR=0.5%	Mean	53.2 (367)	7.57 (52.2)	N/A	N/A	N/A	N/A
	Min	37.7 (260)	6.38 (44)	N/A	N/A	N/A	N/A
	Max	60.8 (419)	9.72 (67)	N/A	N/A	N/A	N/A
	CV(%)	20.1	17.8	N/A	N/A	N/A	N/A
Unreinforced-2 CBR=0.5%	Mean	55.4 (382)	7.32 (50.5)	137.3	10.2	381 (2,630)	N/A
	Min	36.5 (252)	6.09 (42)	132.7	8.5	N/A	N/A
	Max	72.7 (501)	8.41 (58)	141.5	12.7	N/A	N/A
	CV(%)	24.6	11.8	2.4	18.1	N/A	N/A
Unreinforced CBR=8%	Mean	54.9 (378)	8.70 (60.0)	N/A	N/A	N/A	N/A
	Min	41.4 (285)	6.67 (46)	N/A	N/A	N/A	N/A
	Max	64.8 (447)	11.80 (81)	N/A	N/A	N/A	N/A
	CV(%)	26.8	20.8	N/A	N/A	N/A	N/A
GG1 at interface CBR=0.5%	Mean	59.0 (407)	8.85 (61.0)	146.5	6.4	405 (2,792)	1759 (12128)
	Min	47.8 (330)	6.38 (44)	144.2	4.7	N/A	1250 (8618)
	Max	65.3 (450)	10.20 (70)	149.1	7.9	N/A	2570 (17720)
	CV(%)	11.9	13.8	1.0	24.7	N/A	26.6
GG2 at interface CBR=0.5%	Mean	51.2 (353)	7.28 (50.2)	137.0	9.2	431(2,970)	N/A
	Min	45.5 (314)	5.22 (36)	135.3	7.9	N/A	N/A
	Max	61.9 (427)	10.30 (71)	138.2	11.0	N/A	N/A
	CV(%)	12.3	25	1.1	15.3	N/A	N/A
GG3 at interface CBR=0.5%	Mean	55.3 (381)	8.99 (62.0)	146.8	6.2	321 (2,213)	1859 (12817)
	Min	45.0 (310)	8.12 (56)	144.1	4.6	N/A	1380 (9515)
	Max	60.5 (417)	10.20 (70)	149.3	7.9	N/A	2500 (17237)
	CV(%)	11.5	5.4	1.1	16.9	N/A	19.8
GG4 at interface CBR=0.5%	Mean	57.8 (399)	9.69 (66.8)	145.3	6.9	393 (2711)	1499 (10335)
	Min	45.7 (315)	8.70 (60)	143.6	4.8	N/A	1170 (8067)
	Max	68.0 (469)	11.00 (76)	148.7	8.1	N/A	2670 (18409)
	CV(%)	14	5.8	1.1	13.2	N/A	29.3
GG3 at the middle CBR=0.5%	Mean	56.1 (387)	7.31 (50.4)	140.0	9.8	420 (2,899)	1481 (10211)
	Min	51.8 (357)	6.67 (46)	138.0	8.9	N/A	870 (5998)
	Max	59.6 (411)	7.98 (55)	141.3	11	N/A	2410 (16616)
	CV(%)	6.5	6.3	1.2	11.1	N/A	29.7
GG4 at the middle CBR=0.5%	Mean	58.7 (405)	9.96 (68.7)	146.0	6.7	3610 (2,488)	2503 (17258)
	Min	55.6 (384)	8.41 (58)	144.9	5.6	N/A	2020 (13927)
	Max	65.0 (449)	11.00 (76)	147.7	7.4	N/A	2980 (20546)
	CV(%)	6.4	7.4	1.0	14.1	N/A	13.3
GG4 at the upper one third CBR=0.5%	Mean	58.0 (400)	9.47 (65.3)	146.3	6.5	407 (2806)	1951 (13452)
	Min	33.1 (228)	8.12 (56)	145.0	5.1	N/A	1210 (8343)
	Max	73.0 (503)	11.20 (77)	148.1	7.9	N/A	2700 (18616)
	CV(%)	27	7.0	1.1	15.3	N/A	23.7
GG4 at the middle with prime coat CBR=0.5%	Mean	N/A	10.40 (71.5)	146.5	6.3	378 (2,607)	N/A
	Min	N/A	9.14 (63)	145.2	5.2	N/A	N/A
	Max	N/A	11.30 (78)	148.7	7.6	N/A	N/A
	CV(%)	N/A	6.4	1.0	13.7	N/A	N/A

¹E_{GG}=P(1-ν²)/1.77Rδ, P= the applied force, ν=Poisson's ratio, R=outside radius of the Geogauge ring foot, δ=the displacement; ²E_{LFWD}=2(1-ν²)σR/δ_c, σ=the applied stress, R=the loading plate radius of LFWD, δ_c=center deflection of the loading plate; ³ Resilient Modulus; ⁴ Measured by Portable Seismic Pavement Analyzer

Table 8
Summary of Cyclic Plate Load Tests

Reinforcement configuration	Base Thickness inch (mm)	HMA Thickness inch (mm)	Rut depth = 0.75 inch (19.1 mm)				Rut depth = 1 inch (25 mm)			
			Cycles	TBR ^c	TBR ^d	TBR ^e	Cycles	TBR ^c	TBR ^d	TBR ^e
Unreinforced-1 (CBR = 0.5%)	12 (305) ^a	2 (51) ^a	1601	—	—	—	14014	—	—	—
Unreinforced-2 (CBR = 0.5%)	12.7 (323) ^b	2.1 (52.8) ^b	7536	—	—	—	32962	—	—	—
Unreinforced (average) (CBR = 0.5%)	—	—	3887	—	—	—	23340	—	—	—
Unreinforced (CBR = 8%)	12 (305) ^a	2 (51) ^a	—	—	—	—	—	—	—	—
GG1 (interface) (CBR = 0.5%)	12.6 (319) ^b	2.4 (60) ^b	21482	5.5	13.4	2.9	49145	2.1	3.5	1.5
GG2 (interface) (CBR = 0.5%)	12.5 (317.5) ^b	2.2 (55.6) ^b	23628	6.1	14.8	3.1	70427	3.0	5.0	2.1
GG3 (interface) (CBR = 0.5%)	12.8 (325) ^b	2.2 (56) ^b	24872	6.4	15.5	3.3	81362	3.5	5.8	2.5
GG4 (interface) (CBR = 0.5%)	12.2 (311) ^b	2.2 (57) ^b	28735	7.4	17.9	3.8	104223	4.5	7.4	3.2
GG3 (middle) (CBR = 0.5%)	12 (305) ^b	2.2 (57) ^b	22952	5.9	14.3	3.0	50663	2.2	3.6	1.5
GG4 (middle) (CBR = 0.5%)	11.9 (302) ^b	2.3 (59) ^b	26681	6.9	16.7	3.5	59621	2.6	4.3	1.8
GG4 (upper one third) (CBR = 0.5%)	12.2 (310) ^b	2.2 (57) ^b	59560	15.3	37.2	7.9	— ^f	—	—	—
GG4 (middle with prime coat) (CBR = 0.5%)	12.3 (312) ^b	2.2 (57) ^b	47225	12.1	29.5	6.3	— ^f	—	—	—

^aNominal thickness (measured actual thickness is not available for those sections); ^b Measured actual thickness; ^c compared to unreinforced (average) (CBR = 0.5%); ^d compared to unreinforced-1 (CBR = 0.5%); ^e compared to unreinforced-2 (CBR = 0.5%); ^f rut depth in these tests did not reach 1 inch; —: N/A.

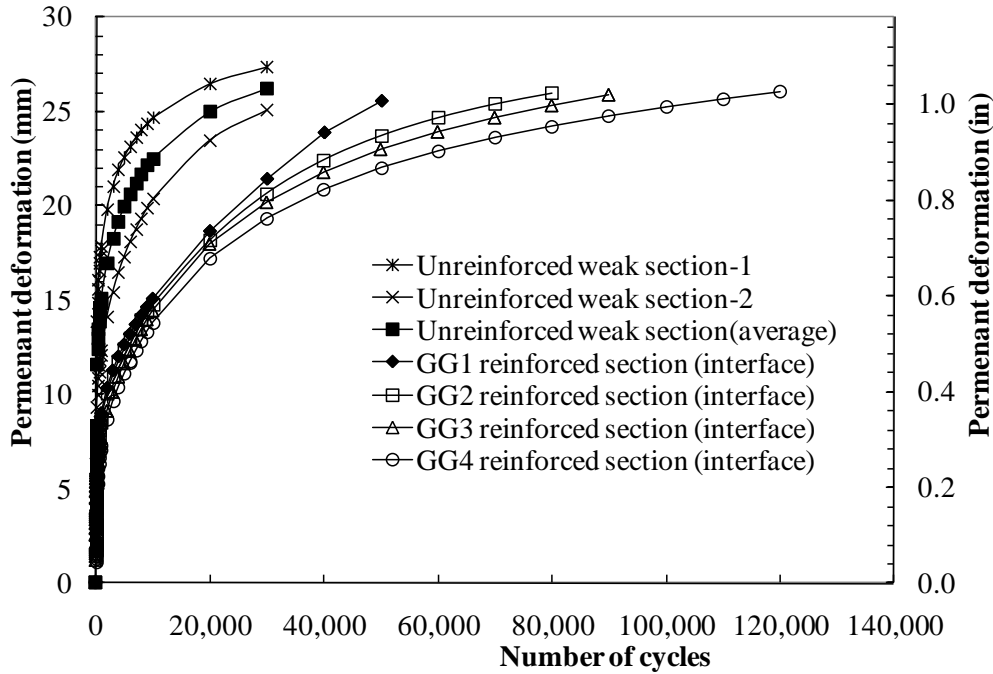


Figure 19
 Development of surface permanent deformation for different types of geogrid placed at base/subgrade interface

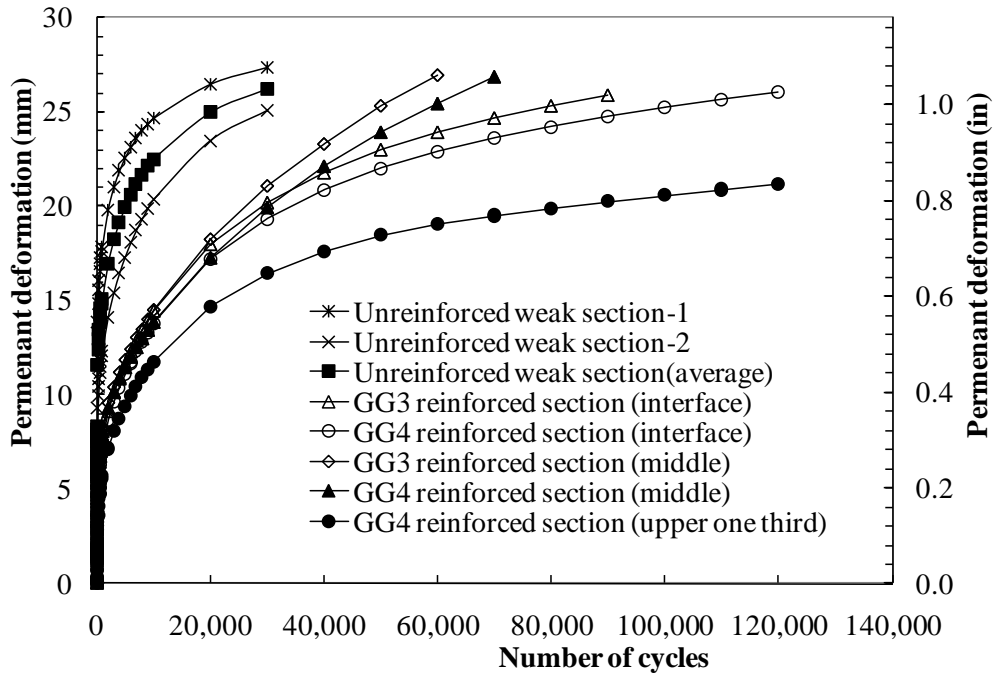


Figure 20
 Development of surface permanent deformation for GG3 and GG4 geogrids placed at different locations

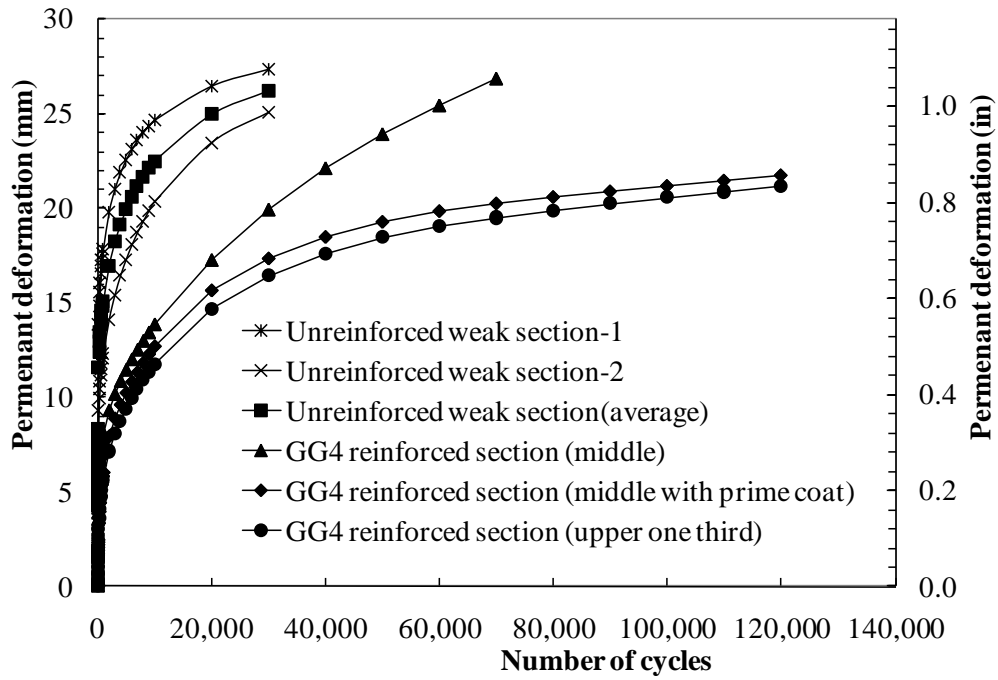


Figure 21
Development of surface permanent deformation for GG4 geogrid placed at the middle of base layer with and without prime coat

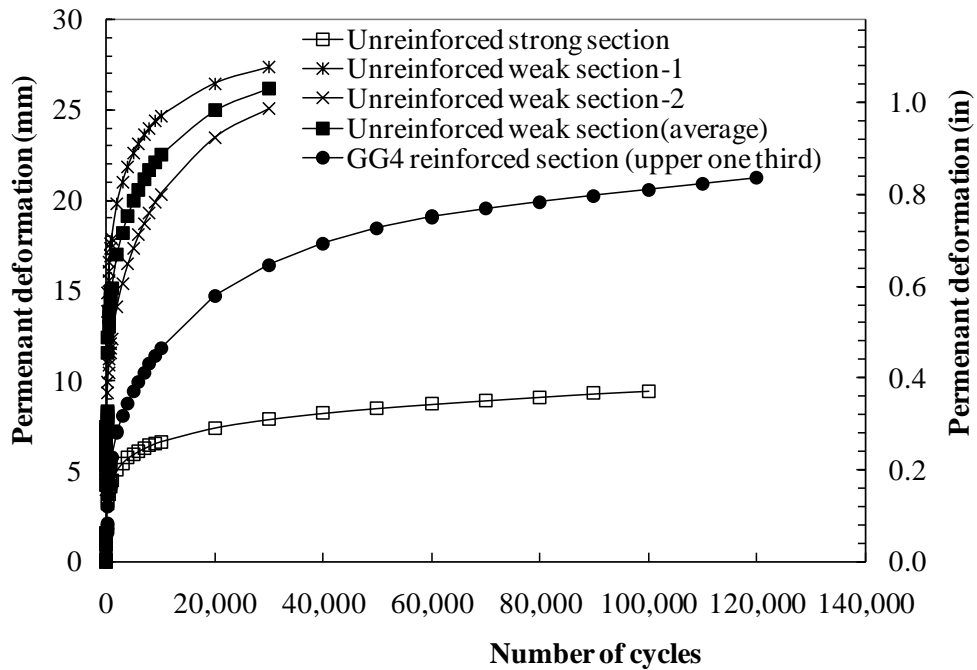


Figure 22
Development of surface permanent deformation for unreinforced weak and strong sections and GG4 reinforced section

Instrumentation. As described earlier, the response time of the Geokon 3500 pressure cell is longer than that of the Kulite 0234 type pressure cell. However, based on the measured data in this study as shown in Figure 23, there is no obvious phase lag between the stress measured by the Geokon 3500 and the applied load.

Most of the strain gages in this study failed after 1000 cycles during the test, except for the strain gages located at distances greater than $1.0 D$ ($D =$ loading plate diameter) from the center of the plate. As expected, the mean strain experienced by the strain gage increased in the tensile direction with time, as shown in Figure 24, because of plastic strain accumulation. The figure also shows that the amplitude of cyclic elastic strain increased with the increase in the number of loading cycles (from 0.23% of cycle 1 to 0.26% of cycle 50).

The fatigue life of the foil strain gage usually decreases as the amplitude of the cyclic elastic strain increases. A mean-strain increase in a tensile direction during cycling will also lead to a much shorter fatigue life. At the 1000th cycle, the strain gage located directly below the center of plate, experienced about 0.5% permanent strain, was subjected to a dynamic strain level of 4000 $\mu\epsilon$. Recent conversations with representatives from Vishay Micro—Measurements indicated that no bondable foil strain gages can survive for long periods at such high amplitude of cyclic elastic strains with the permanent strain increasing in the tensile direction. This limitation of bondable foil strain gages motivated the authors to look for a new instrumentation strategy to better measure the strain distribution along the geogrids in future tests.

Surface Deformation and Contour

Figure 19, Figure 20, Figure 21, and Figure 22 illustrate the development of rut depth (permanent deformation) with number of load cycles for the different tested pavement sections. The permanent surface deformation was calculated by averaging the readings of the two LVDTs sitting on top of the loading plate. The results show the trend that the permanent deformation accumulated with the increase in the number of load cycles. The rut depth increase was fast at the early stage of the loading cycles; however, the rate of increase in rut depth decreased with the increase in the number of load cycles. By comparing the reinforced sections with the unreinforced sections, one can observe the benefit of geogrid base reinforcement on the rutting behavior of the pavement sections. For example, at 30,000 loading cycles, the total deformation decreased from 1.03 in. (26.2 mm) for the average of unreinforced weak sections down to 0.65 in. (16.4 mm) for the geogrid reinforced section (GG4 geogrid placed at the upper one third of the base layer). The corresponding TBR values determined for the different geogrid base reinforced sections at the rut depth of 1 in. (25.4 mm), as shown in Table 8, are greater than 2.1. Figure 22 also shows that the unreinforced

pavement section on strong subgrade performed much better than reinforced sections on weak subgrade. This suggests that the strength of subgrade is crucial to the performance of geogrids reinforcement in pavement systems.

The profiles of surface deformation were measured using the eight LVDTs described in Figure 12. Figure 25 demonstrates that the reinforced sections exhibited lower levels of surface deformations than the unreinforced sections tested on same subgrade strength. The figure also shows that a small amount of tilt occurred in the loading plate. This may be due to local variations in the properties of the HMA, the base course, or the subgrade.

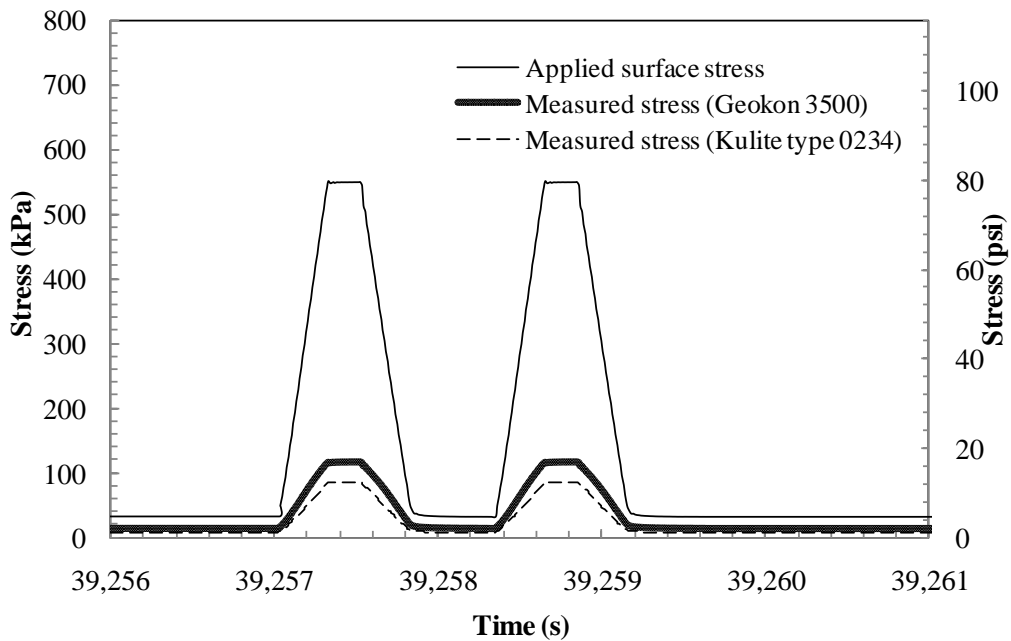


Figure 23
Typical response of pressure cells

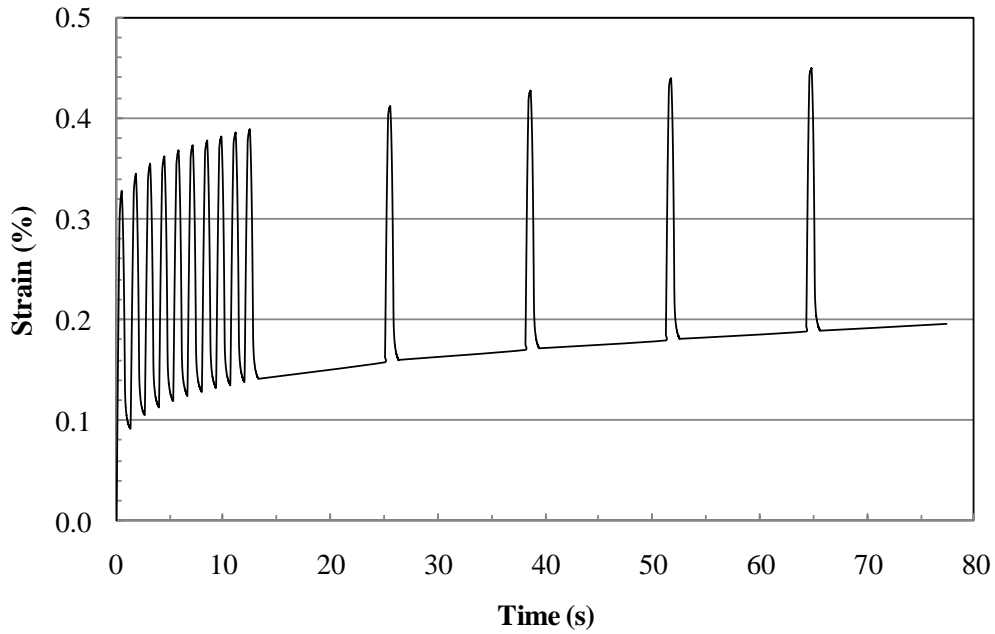


Figure 24
Typical response of strain gauge

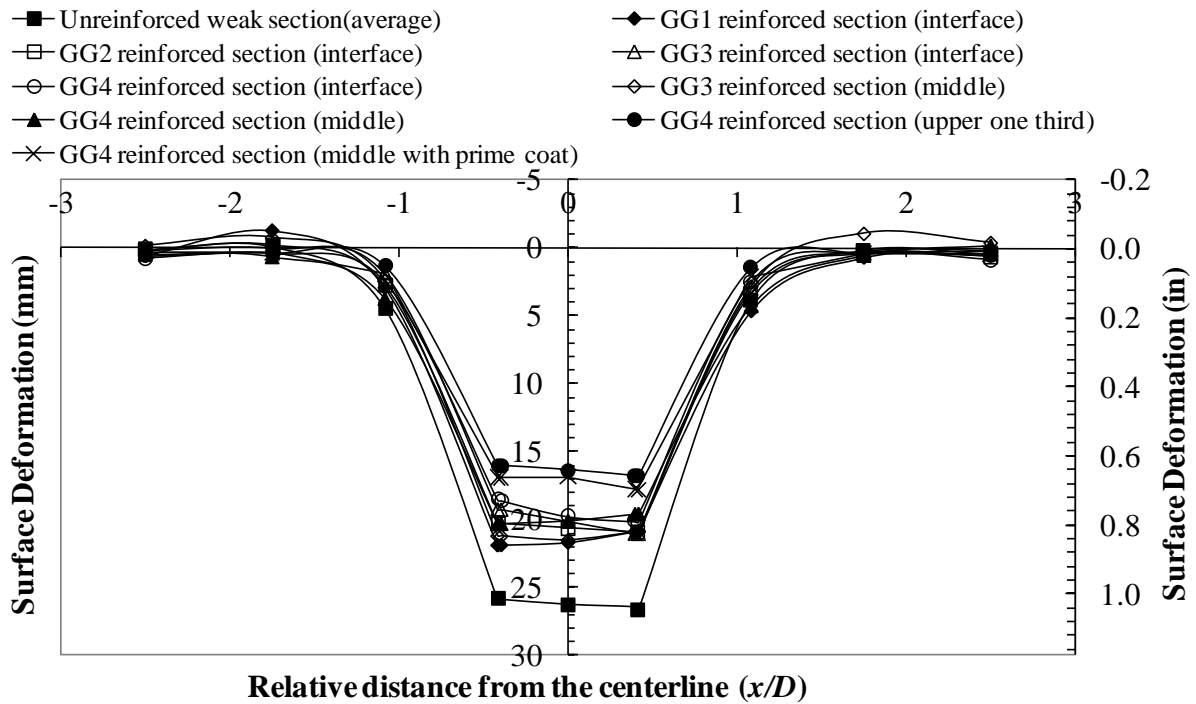


Figure 25
Profile of surface deformation at N = 30,000

Effect of Properties and Type of Geogrid

Four different types of geogrids were used in this study. The properties of these geogrids were presented earlier in Table 1. The GG1 and GG2 geogrids are made of the same material and have similar aperture size, but GG2 has a higher tensile modulus than GG1 (Table 1). Figure 19 shows that the pavement section with GG2 geogrid base reinforcement performed better than the section with GG1 geogrid reinforcement. The same observation was also obtained for GG3 and GG4 geogrids (same material and similar aperture size). Overall, the improvement in the performance of pavement sections increases as the tensile modulus of the geogrid increases (Figure 19). Meanwhile, no clear relationship was observed between the performance and the aperture stability modulus of the geogrid in this study although Giroud and Han (2004) selected this property instead of tensile modulus of geogrid to develop their design method for unpaved road. The triaxial geogrid GG3 performed better than the biaxial geogrid GG2, which has a similar tensile modulus but with a different aperture shape (geometry) compared to the GG3 geogrid. For the conditions examined in this study, the TBR was increased from 6.1 for the biaxial geogrid GG2 to 6.4 for the triaxial geogrid GG3 at a rut depth of 0.75 in. (19 mm).

Effect of Location of Geogrid

The effect of geogrid location was investigated by using GG3 and GG4 geogrids. The following reinforcement configurations were selected to study this effect: placing geogrid at the base/subgrade interface, at the middle of the base layer, and at the upper one third of the base layer. It can be seen from Figure 20 that the pavement section with geogrid placed at the upper one third of the base layer has the best performance, followed by the pavement section with geogrid placed at the subgrade/base interface, and then by the pavement section with geogrid placed at the middle of base layer.

It should be mentioned here that for pavement sections with geogrid placed at the middle of base layer, the geogrid was laid on top of a 6-in. (152-mm) thick compacted limestone aggregate layer. Loose limestone aggregate was then placed over the geogrid and compacted to the target density. For pavement section with a geogrid layer placed at the upper one third of the base layer, the geogrid was laid on top of a layer of loose limestone aggregate [2 in. (51 mm) thick in compacted state] and sandwiched by another layer of loose limestone aggregate [4 in. (102 mm) thick in compacted state] over it. Both crushed limestone layers were then compacted together to the target density.

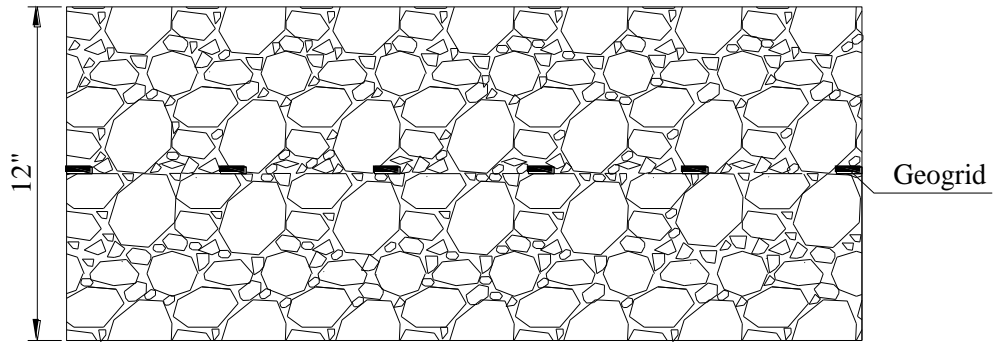
In the general construction procedure, the support soil layer (i.e., the soil placed under the geogrid) is usually compacted to the target density. Next, the geogrid is laid on top of this compacted soil layer. Then, the confined soil layer is placed over the geogrid. When the

confined soil layer is compacted over the geogrid, two cases need to be identified and discussed:

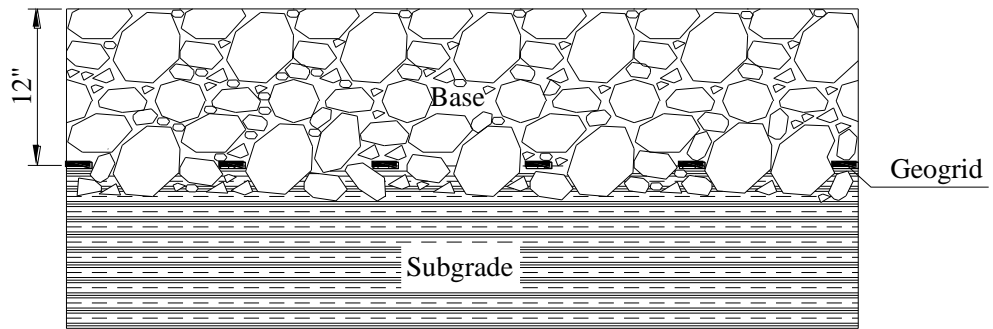
1. If both the support and confined soil layers of the geogrid are crushed limestone aggregate (i.e., geogrid placed within the base layer), then it is difficult for the crushed limestone aggregate of the confined layer to partially penetrate and project through the geogrid apertures during the compaction process because the support layer has approximately smooth surface, as shown in Figure 26a. As such, it is difficult to create the adequate geogrid-base interlocking needed to mobilize the geogrid reinforcement. This might explain why the geogrid placed at the middle of base layer did not perform well in this study.
2. When the geogrid is placed at the base-subgrade interface, it is relatively easy for the crushed limestone aggregate of the confined layer to partially penetrate and project through the geogrid apertures during the compaction process to create the adequate geogrid-base interlocking needed to mobilize the geogrid reinforcement, as shown in Figure 26b.

A new construction technique was implemented in this study for the geogrid placed at the upper one third of the base layer to improve the interlocking between the geogrid and the crushed limestone aggregate. The geogrid was laid on top of loose support aggregate layer [2 in. (51 mm) thick in compacted state] and then sandwiched by the upper confined aggregate layer 4 in. (102 mm) thick in compacted state]. Both the support and the confined aggregate layers were compacted together so that the crushed limestone aggregates can partially penetrate and project through the geogrid apertures, as shown in Figure 26c. This construction technique achieved very promising results. The enhanced performance can be seen in Figure 20, which shows that the pavement section with the geogrid placed at the upper one third of the base layer performed significantly better than the rest of the pavement sections.

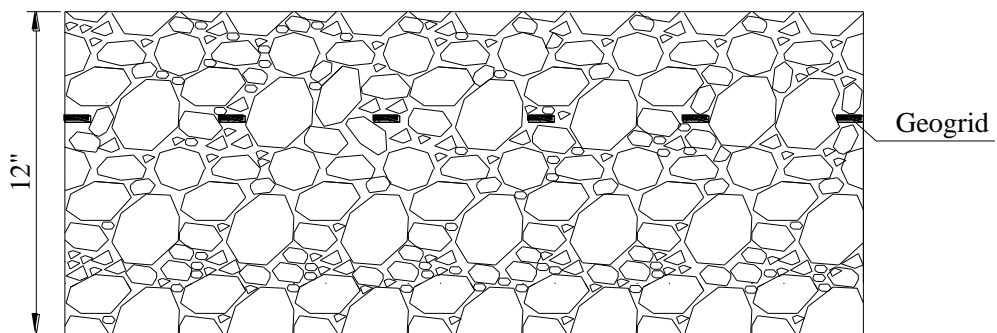
To improve the interaction between geogrid and the crushed limestone aggregate for geogrid placed at the middle of base course layer, a prime coat was applied to the surface of the compacted support layer before placing the geogrid to promote bonding with the subsequent confined layer. As such, adequate geogrid-base interaction could be created. Very encouraging results were achieved using this construction technique. The enhanced performance can be easily seen in Figure 21, which shows that the pavement section with prime coat applied to the compacted support layer performed significantly better than that without the application of prime coat. The TBR was increased from 6.9 to 12.1 at a rut dept of 0.75 in. (19 mm) (Table 8).



(a) geogrid placed at the middle of base course layer (base course reinforcement)



(b) geogrid placed at the base/subgrade interface (subgrade stabilization)



(c) geogrid placed at the upper one third of base course layer (base course reinforcement)

Figure 26
Possible configurations at the geogrid interface

Stress Distribution and Vertical Permanent Strain within Subgrade

The vertical stress distribution at 3 in. (76 mm) below the subgrade/base interface and along the centerline of the loading plate obtained at the end of 30,000 cycles for both geogrid reinforced and unreinforced weak sections are shown in Figure 27. The measured stresses represent the total vertical stresses induced by the peak load during each cycle (the stresses induced by the weight of soil are not included). The figure demonstrates that, when geogrids

were included, the load was redistributed over a wider area within the reinforced test sections, resulting in an improved stress distribution on top of the subgrade layer. The magnitude of vertical stress was decreased directly below the plate and increased slightly away from the plate in the reinforced test sections compared to the unreinforced sections.

Among all pavement sections, the pavement section with GG4 geogrid placed at the upper one third of the base layer, which has the best performance in terms of TBR, provided the best attenuation of the vertical stress on top of the subgrade below the center of loading. In general, the higher the geogrid tensile modulus, the higher the reduction in the maximum vertical stresses on top of the subgrade under similar conditions.

The improved stress distribution leads to less accumulation of permanent deformation in the subgrade layer. Figure 28 presents the permanent vertical strain accumulated in the subgrade layer beneath the center of the loading plate. Although no permanent vertical strain was measured for the unreinforced section due to the fact that a soil strain gage was not available at that time, it still can be seen from Figure 27 and Figure 28 that the permanent vertical strain in the subgrade is directly related to the vertical stress, i.e., the lower the maximum vertical stress on top of the subgrade, the lower the permanent vertical strain in the subgrade.

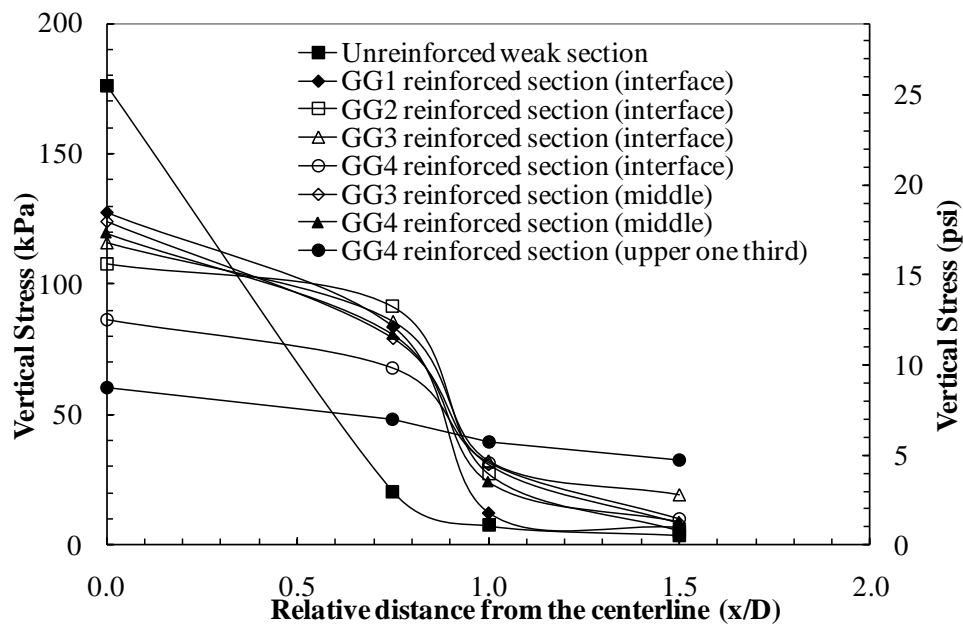


Figure 27
Vertical stress distribution at N = 30,000 [at 3 in. (76 mm) below the top of subgrade]

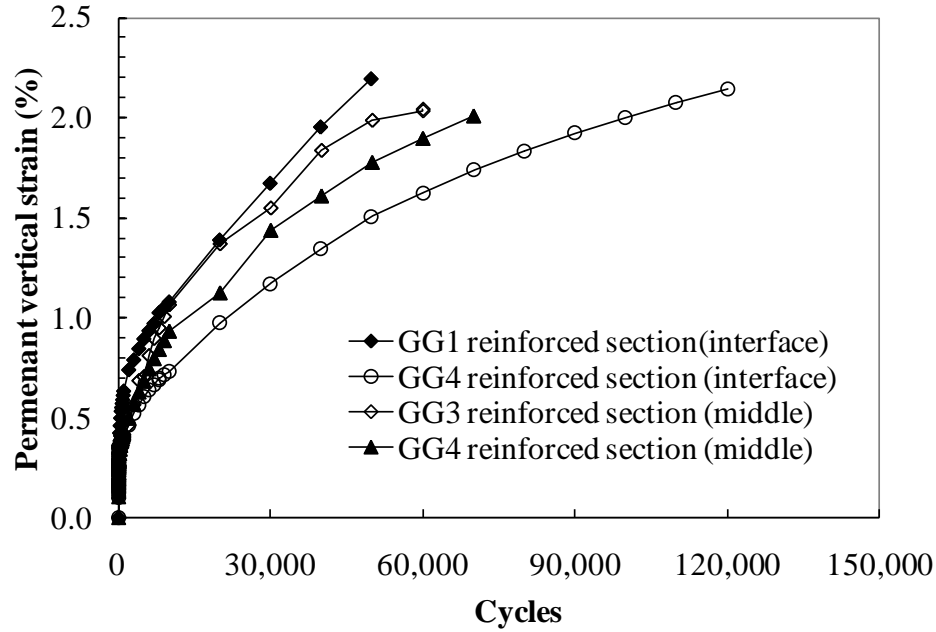
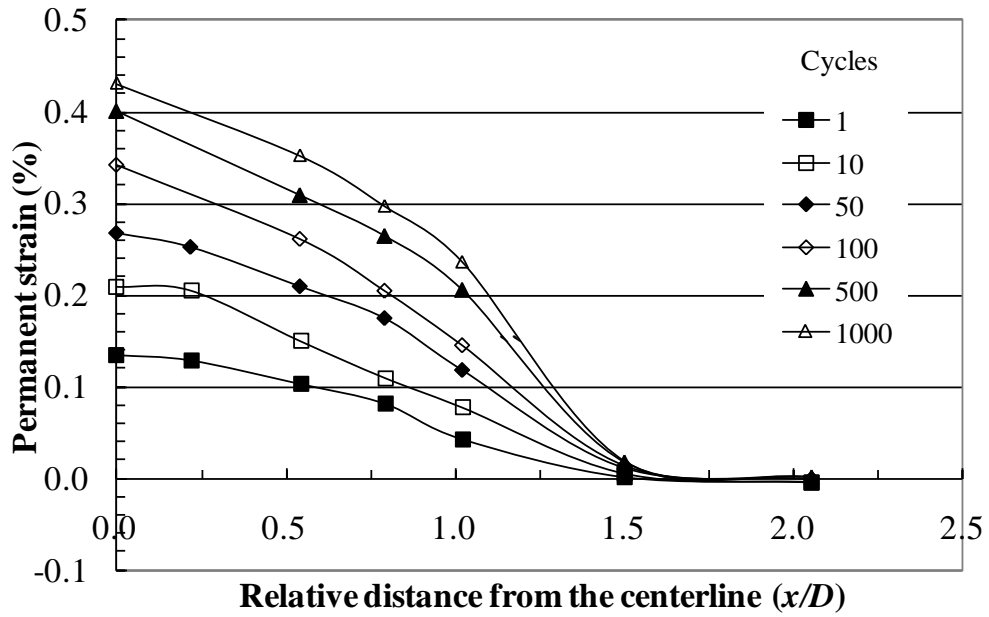


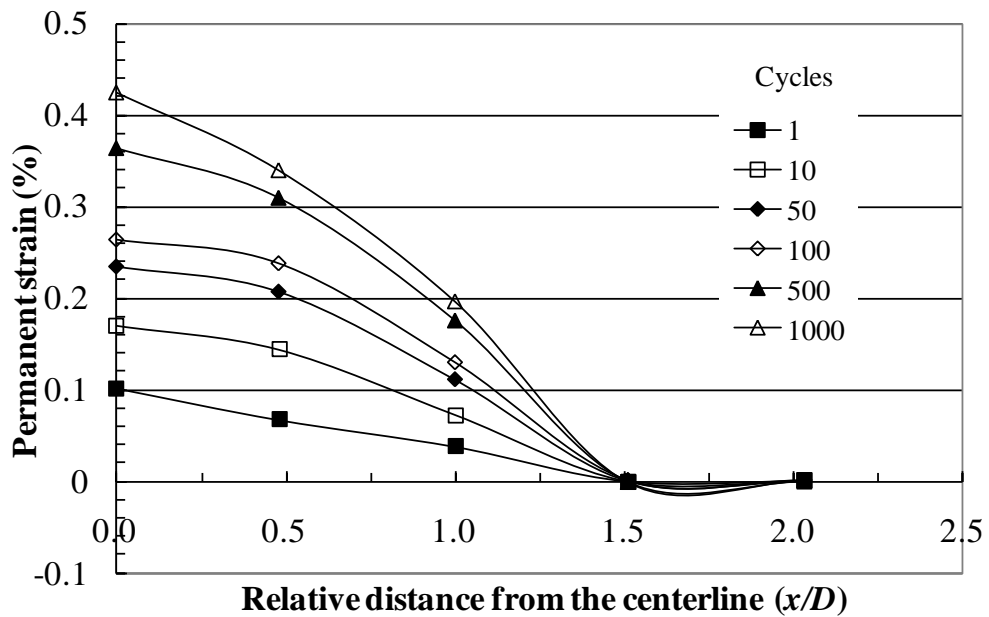
Figure 28
Permanent vertical strain in the subgrade versus load cycle [at 3 in. (76 mm) below the top of subgrade]

Strain Distribution along the Geogrid

The variations of strains measured along the centerline of the geogrids for different load cycles are presented in Figure 29 through Figure 33. Under cyclic load testing, the strain gages experienced both accumulation of residual (plastic) strains and relatively high dynamic strain level, causing them to stop working after about 1000 loading cycles. As such, the figures only present the strain distribution up to 1000 cycles. The figures showed that significant permanent tensile strains were developed in the geogrids, which are believed to restrain the lateral movement of the base course aggregates. The highest measured tensile strains were observed at the point beneath the center of the loading plate, where the maximum lateral movements of the base course aggregates were expected to occur, and became almost negligible at a certain distance. This distance is about $1.5 D$ (D : loading plate diameter) from the center of the loading plate for geogrid placed at the subgrade/base interface, and about $1.0 D$ from the center of loading plate for geogrid placed at the middle of the base course layer. The maximum measured strains in geogrids were well below the failure strains for geogrids. The figures also show that the permanent strains are almost similar for different geogrids placed at the same location.

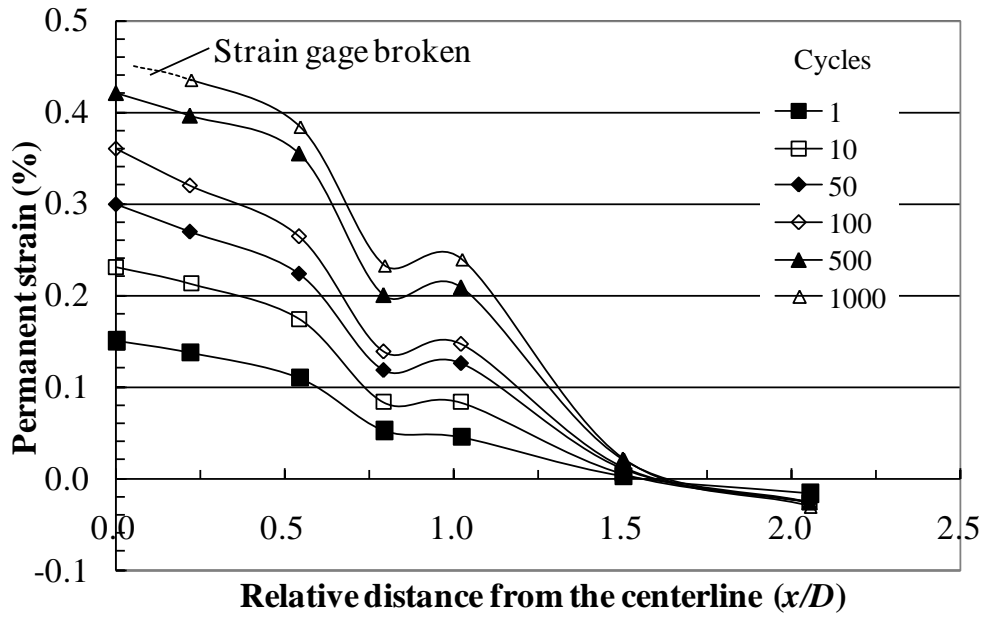


(a) Machine direction

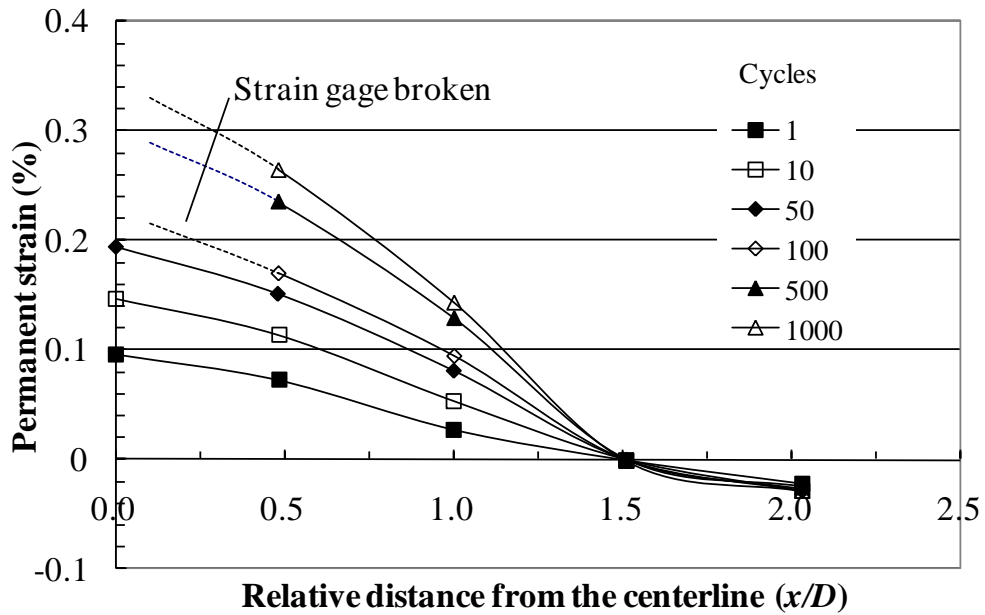


(b) Cross machine direction

Figure 29
Permanent strain distribution along the centerline of GG1 geogrid placed at the base/subgrade interface (D : loading plate diameter)



(a) Machine direction



(b) Cross machine direction

Figure 30
Permanent strain distribution along the centerline of GG2 geogrid placed at the base/subgrade interface (D : loading plate diameter)

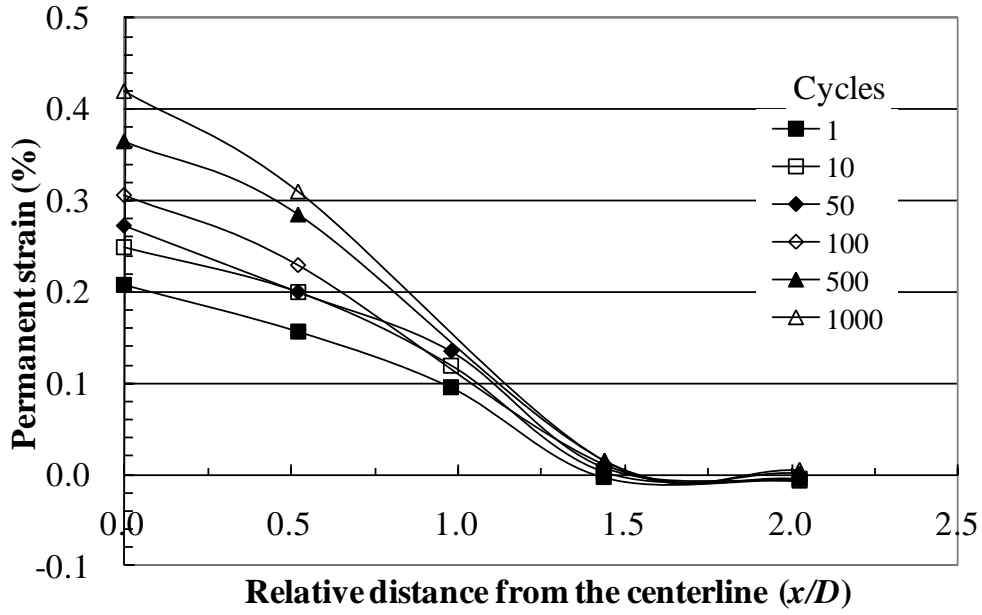


Figure 31
Permanent strain distribution along the centerline of GG3 geogrid placed at the base/subgrade interface (D : loading plate diameter)

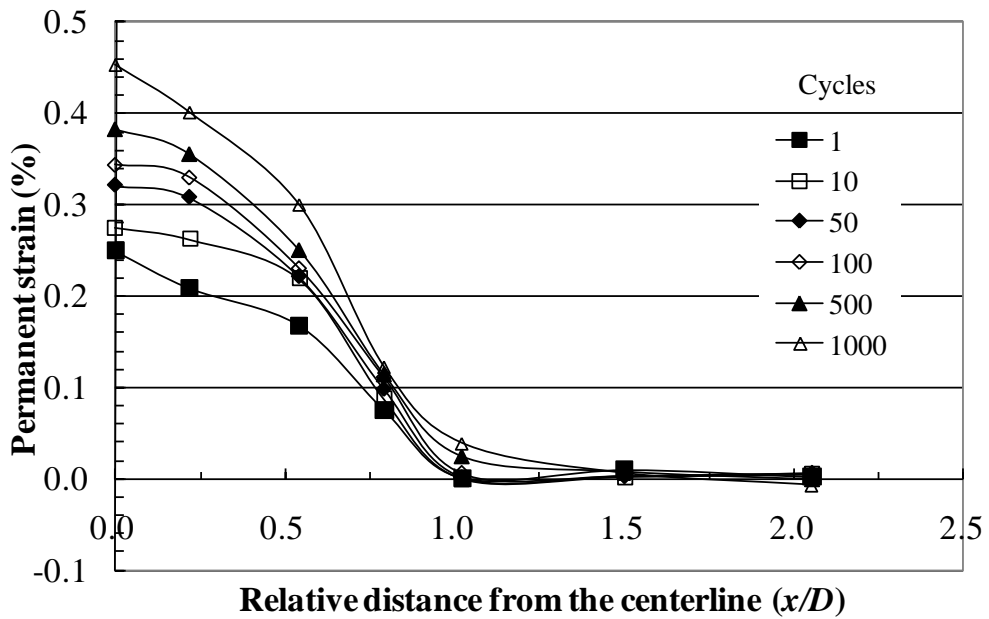


Figure 32
Permanent strain distribution along the centerline of GG3 geogrid placed at the middle of base layer (D : loading plate diameter)

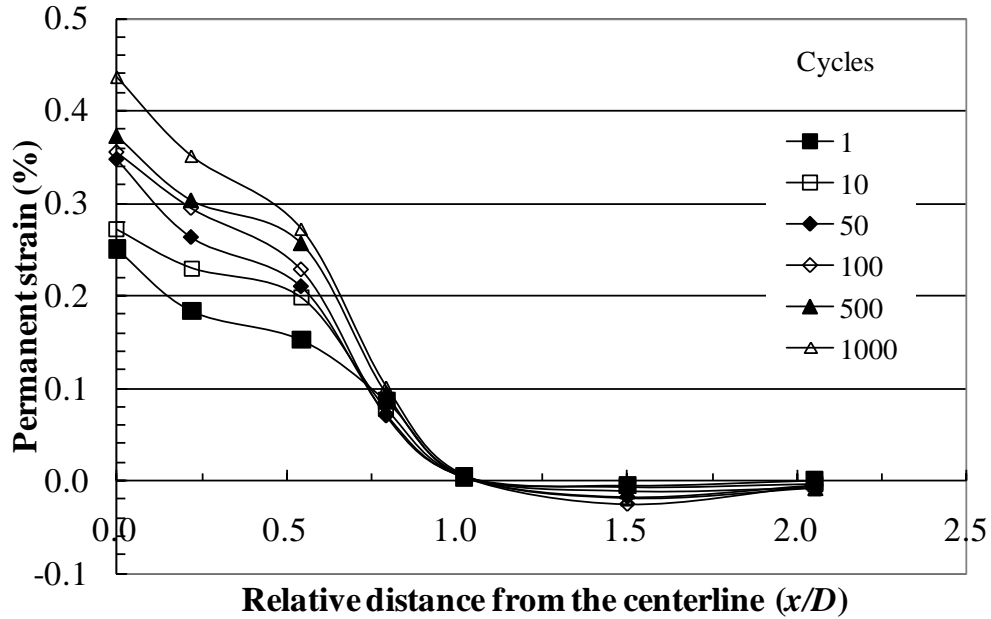


Figure 33
Permanent strain distribution along the centerline of GG4 geogrid placed at the middle of base layer (D : loading plate diameter)

Pore Water Pressure within Subgrade

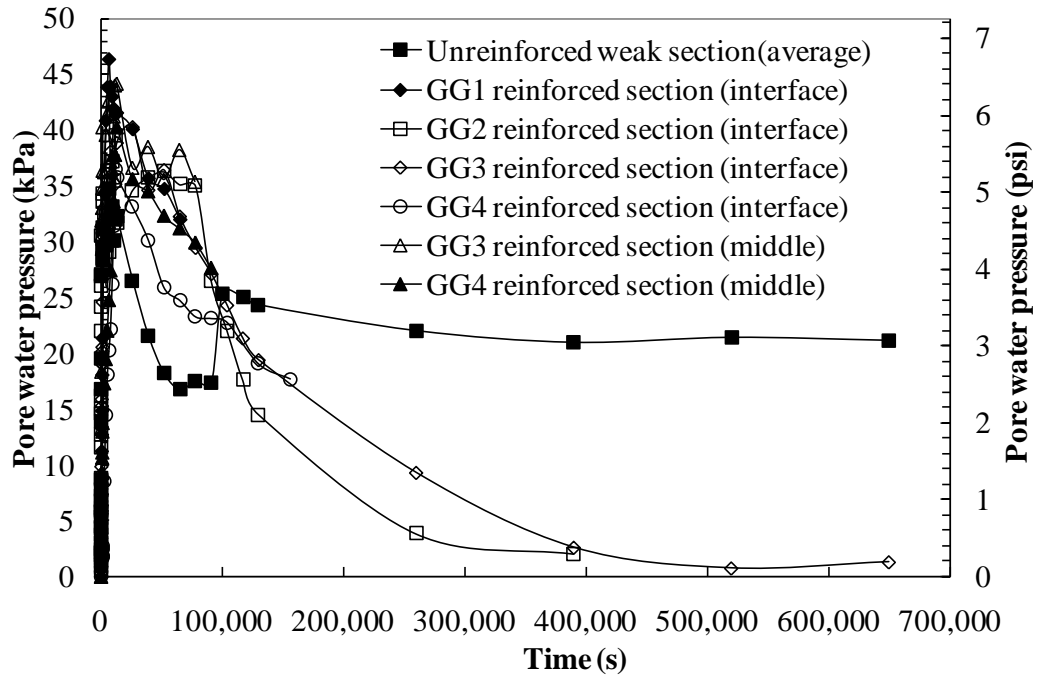
The development of pore water pressure for geogrid reinforced and unreinforced pavement sections measured at the point directly below the center of the plate are shown in Figure 34a. It is interesting to notice that the pore water pressure was initially built up at a relatively fast rate until reaching a peak value, followed by gradual dissipation after that. This trend is similar to that of the amplitude of the cyclic elastic surface deformation as shown in Figure 34b. Several researchers showed that the generation of excess pore water pressure in the soil is controlled mainly by the amplitude of cyclic shear strain during cyclic loading [39]. For a given soil, there exists threshold cyclic shear strain amplitude above which the excess pore water pressure accumulates with the number of cycles and below which such an accumulation does not occur. The cyclic shear strain amplitude within the subgrade should be somehow related to the amplitude of the cyclic elastic surface deformation of the pavement. A similar trend between the pore water pressure and the amplitude of cyclic elastic surface deformation is explained below.

As shown in Figure 34b, the amplitude of cyclic elastic surface deformation was initially larger than the threshold value, in which the excess pore water pressure accumulated continuously with the number of cycles, and rapidly increased to the peak value. Thereafter,

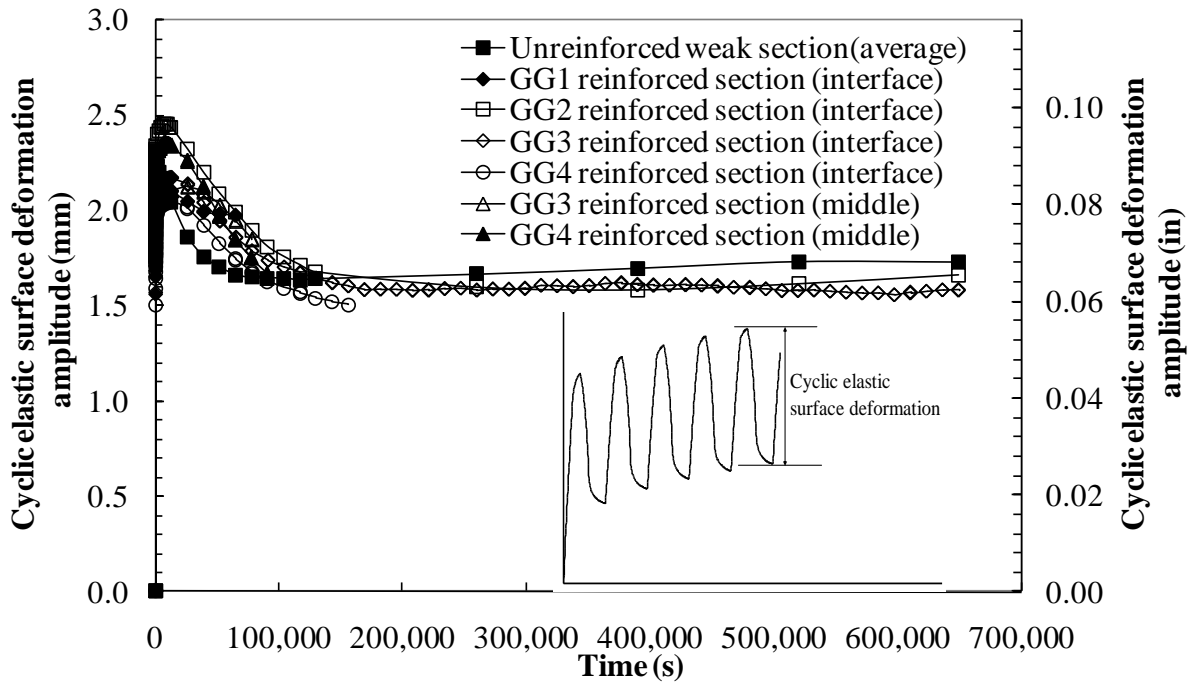
the amplitude of cyclic elastic surface deformation gradually decreased below the threshold value, in which the excess pore water pressure did not accumulate with the number of cycles. Meanwhile, the excess pore water kept dissipating toward the outside area. For the unreinforced section (Figure 34a), after initial increase and decrease in the excess pore water pressure, the pore water pressure started increasing again at around 100,000 s. This observation is consistent with the change of the amplitude of cyclic elastic surface deformation at this time as shown in Figure 34b.

General Comments

In this study, the benefits of using geogrid base reinforcement to reduce the rut depth of the pavement sections has been clearly demonstrated through the results of laboratory cyclic plate load tests on reinforced test sections. As compared to the stationary cyclic plate load test that applies vertical concentrated load, the real traffic involves moving wheel loads with wander. As such, the performance of geogrid base reinforcement due to real traffic loads could be different from that due to stationary cyclic plate loads. Under a rolling wheel load, a pavement element within the plane of the wheel track experiences various combinations of vertical, horizontal, and shear stresses with an extension-compression-extension multiple stress path and continuous rotation of the principal stresses. Both extension-compression-extension multiple stress path loading and traffic wander can cause the recurring movement and rearrangement of the particles and, thus, result in a dramatic degradation of the unbound aggregate layer, which reduces the strength of the unbound materials [23, 29]. This degradation of unbound aggregates causes more permanent deformation with future load applications, or even may cause shear failure of the base layer. Placing geogrid at the base-subgrade interface or within the base course layer should be able to minimize the recurring movement and rearrangement of the particles. Accordingly, the benefits of geogrid base reinforcement in the field could be more significant than demonstrated in the laboratory cyclic plate load tests of this study.



(a) Pore water pressure (at 152 mm below the top of subgrade)



(b) Cyclic surface deformation amplitude

Figure 34
Development of pore water pressure and amplitude of cyclic surface deformation at the center

Field Load Tests on Various Base/Subbase Materials

Test Results

In-Place Properties. Large variation can exist on the strength/stiffness properties of the pavement layers from time of construction to time of testing. As such, the DCP, FWD, and Dynaflect were deployed to evaluate the in-situ strength/stiffness of the field test lane sections at the time when the rolling wheel load tests were performed and at the time when the cyclic plate load tests were performed. Table 9 summarizes the mean values of the field tests obtained for the seven test lane sections.

As can be seen from DCP data, the in-situ stiffness of cementitiously stabilized soils (lime and cement treated) under cyclic plate loads are significantly higher than those values under rolling wheel loads due to the time gap between the rolling wheel load tests and the cyclic plate load tests (Table 9Table 9). This aging effect will be further discussed in the subsection “aging effect.” A slight increase of in-situ stiffness was also observed in the base layers from the DCP test data, but the increase in stiffness of the base layers from the time of rolling wheel load tests and the time of cyclic plate load tests is not significant compared to the subbase layers. Both the DCP and the Dynaflect data show that the difference in stiffness of the subgrade layer from the time of rolling wheel load tests and the time of cyclic plate load tests is insignificant. Meanwhile, the FWD data indicated that the overall stiffness of the 100%RAP/FA+CTS section significantly decreased with time. This may be caused by weakening the section caused by water seepage through the cracks, which will be discussed later.

Validation of Cyclic Plate Load Test. Two cyclic plate load tests were conducted on the 100%RAP/FA+CTS section to check the repeatability of the cyclic plate load test equipment. The development of rutting with the number of ESALs is shown in Figure 35. It can be seen from the figure that the repeatability of the cyclic plate load test is within the acceptable range. The number of cycles under a particular load is converted to the number of ESALs using a generalized fourth power law, as show in equation (1).

$$ESALs = N \times \left(\frac{P}{9000lb} \right)^4 \quad (1)$$

where, N is the number of load cycles under a particular load of P .

A similar pavement section consisted of a 2-in. (51-mm) HMA top layer, a 8.5-in. (216-mm) limestone base layer, a 12-in. (305-mm) lime treated soil subbase layer, and a similar subgrade layer was constructed in a steel test box in the laboratory. The comparison of the

rutting development curves between the field and laboratory cyclic plate load tests on the similar pavement sections is presented in Figure 36. As can be seen from the figure, the development of the rutting curves followed the same trend for both the field cyclic plate load test and laboratory cyclic plate load test. Stiffer response was observed in the field cyclic plate load test. It is worth mentioning here that the field plate load test was conducted more than three years after the construction of the pavement section; while the laboratory plate load test was conducted immediately after section construction. The aging effect can be an important factor as will be discussed later. It can be concluded that the cyclic plate load test, in general, can provide consistent results.

Cyclic Plate Load Tests. The development of rutting with the number of ESALs under the field cyclic plate load is shown in Figure 37. It can be seen from the figure that the performance of the seven pavement sections can be divided into four groups in terms of the rutting behavior. The BCS/slag+LTS and BCS/fly ash+LTS sections have the best performance, followed by the LS+CTS, LS+LTS, and 50%RAP50%SC/FA+CTS sections, then followed by the 100%RAP/FA+CTS section, and finally the BCS+LTS section.

Rolling Wheel Load Tests. The development of rutting with the number of ESALS under the rolling wheel load is shown in Figure 38. In this study, the rolling wheel load test was stopped when the pavement condition reached either of the following failure criteria: (1) rutting failure: when the rut depth reached 0.5 in. (12.7 mm) or (2) cracking failure: when 50 percent of the trafficked area developed visible cracks (e.g. longitudinal, transverse, and alligator cracks) more than 5 m/m² (1.52 ft/ft²). As seen from the figure, the performance of six pavement sections again can be divided into four groups in terms of the rutting behavior. The BCS/slag+LTS section has the best performance, followed by the BCS/fly ash+LTS section, then followed by the LS+CTS, 100%RAP/FA+CTS, and 50%RAP50%SC/FA+CTS sections, and finally the LS+LTS section. It should be mentioned here that the rolling wheel load test stopped at a rut depth of about 0.35 in. (9 mm) for section 100%RAP/FA+CTS as it reached the cracking limit. The other five pavement sections were considered to fail due to rutting. Cracking failure behavior of the pavement sections is beyond the scope of this report.

Table 9
In-place properties

Section	1		2		3		4		5		6		7	
	BCS + LTS		BCS /fly ash + LTS		BCS/slag + LTS		LS + LTS		LS + CTS		100%RAP /FA+ CTS		50%RAP 50%SC/FA + CTS	
	WL ¹	PL ²	WL ¹	PL ²	WL ¹	PL ²	WL ¹	PL ²	WL ¹	PL ²	WL ¹	PL ²	WL ¹	PL ²
	DCP Index (mm/blow)													
Base	4.5	3.4	1.8	1.5	0.3	N/A	3.9	2.1	2.0	3.3	2.0	2.4	4.8	3.0
Subbase	10.9	2.9	8.0	6.4	11.9	5.7	9.6	1.9	6.1	1.8	4.3	1.2	4.3	1.6
Subgrade	15.5	14.0	23.8	33.5	22.0	16.2	18.0	19.0	16.8	17.4	10.6	19.1	22.9	23.5
	DYNAFLECT													
SN ³	N/A	4.1	3.3	3.8	3.9	3.6	1.8	3.5	2.5	3.4	4.0	3.9	3.6	3.6
M _r (ksi) ⁴	N/A	4.1	4.2	4.1	4.0	4.0	3.2	4.0	3.4	4.1	3.9	4.4	4.3	4.2
M _r (MPa) ⁴	N/A	28.3	29.0	28.3	27.6	27.6	22.1	27.6	23.4	28.3	26.9	30.3	29.6	29.0
	Falling Weight Deflectometer (FWD)													
D ₀ , mills ⁵	N/A	14.0	18.1	9.71	9.13	9.44	15.9	15.3	13.8	14.8	7.9	19.3	22.6	13.4
D ₆ , mills ⁵	N/A	3.01	3.66	3.47	3.49	3.19	3.49	4.21	3.29	3.92	2.53	3.09	3.31	2.81
D ₇ , mills ⁵	N/A	2.54	3.07	2.78	2.97	2.66	2.89	3.33	2.80	3.16	2.23	2.59	2.81	2.40
D ₈ , mills ⁵	N/A	2.17	2.53	2.34	2.51	2.30	2.45	2.79	2.37	2.62	1.89	2.24	2.35	2.10

¹WL: rolling wheel load; ²PL: cyclic plate load; ³SN: structure number; ⁴resilient modulus of subgrade; ⁵maximum deflection at 9000 lbf load, expressed in thousandths of inches.

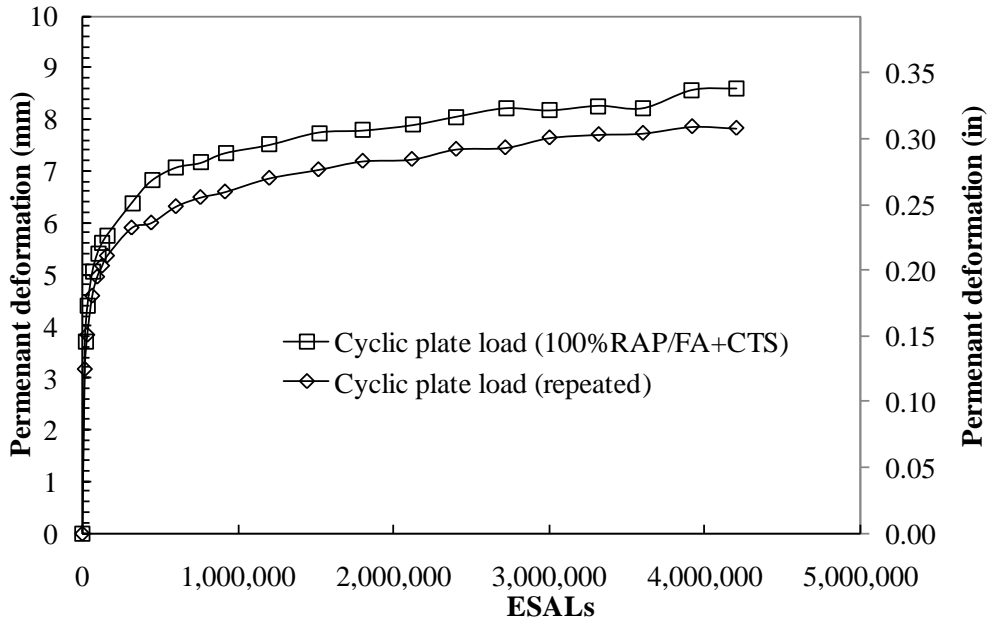


Figure 35
Development of rut depth for repeatability check using the cyclic plate load test

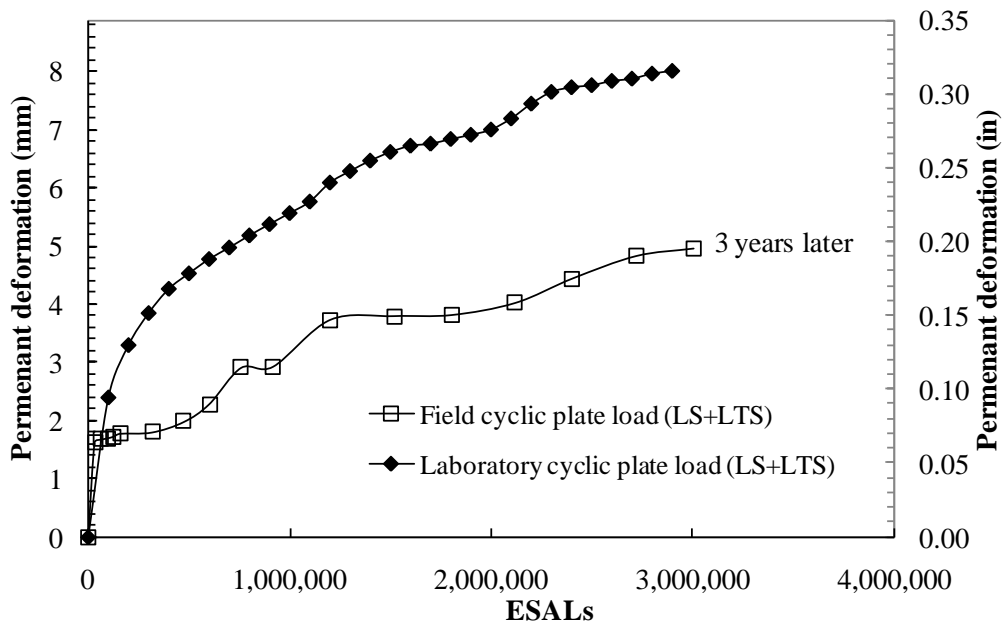


Figure 36
Comparison of field and laboratory cyclic plate load test

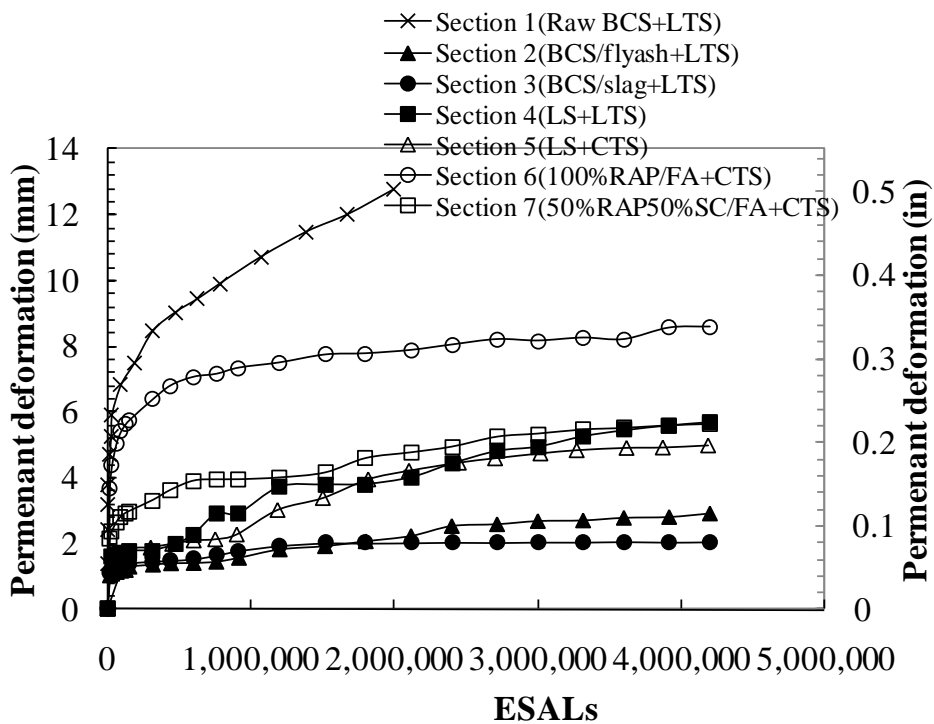


Figure 37
Development of rut depth for cyclic plate load test

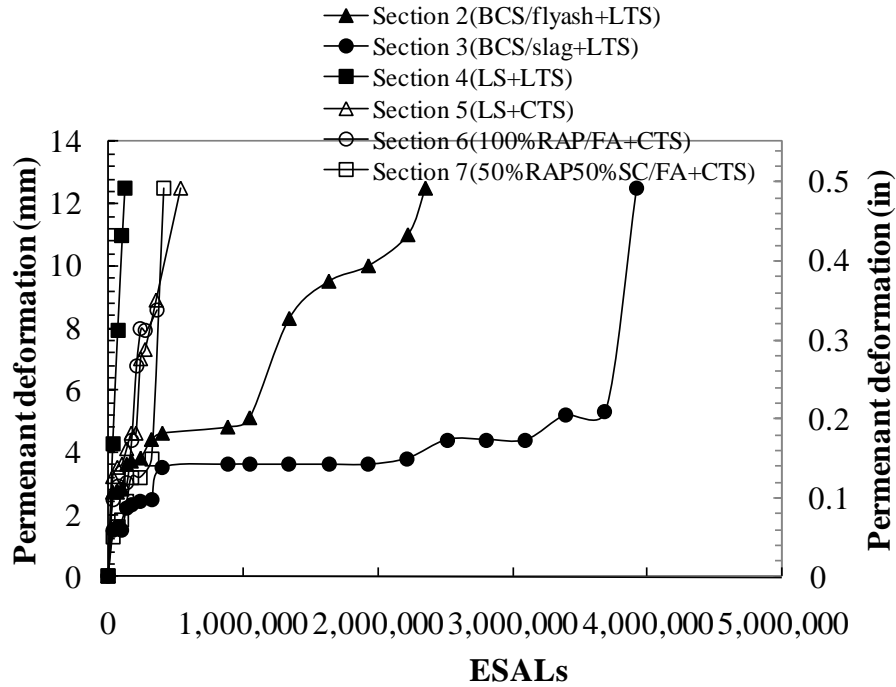


Figure 38
Development of rut depth for rolling wheel load test

Comparison of Various Sections

Equivalent Modulus of Elasticity. All sections consisted of a similar HMA top layer and similar subgrade layer. Base and subbase layer materials varied between the different sections, and various combinations of base and subbase materials were used in the pavement testing sections. Hence, a performance indicator, which can combine the effects of the base and subbase layers, is needed to qualitatively rank the performance of each section. The equivalent modulus of elasticity of the base and subbase layers can be used as an indicator. However, conventionally, only the thicknesses of individual layers are taken into consideration in the evaluation of the equivalent modulus of elasticity or stiffness for a layered system, and the relative position of individual layer is ignored. Equation (2), which is adopted in the reference manual of the National Highway Institute training course: Introduction to Mechanistic-Empirical Pavement Design, is one example [40].

$$E_{eq} = \left(\frac{E_{base}^{1/3} h_{base} + E_{subbase}^{1/3} h_{subbase}}{h_{base} + h_{subbase}} \right)^3 \quad (2)$$

where, E_{eq} is the equivalent elastic modulus of the base and subbase layers; E_{base} is the elastic modulus of the base layer, $= M_{r(base)}$; h_{base} is the thickness of the base layer; $E_{subbase}$ is the elastic modulus of the subbase layer, $= M_{r(subbase)}$; and $h_{subbase}$ is the thickness of the subbase layer.

Equation (2) has a serious limitation since the applied stress decreases with depth, i.e., the effect of external load decreases with depth [41, 42]. This means that the modulus of elasticity or stiffness of the upper layer (base) is more relevant to pavement performance than that of the lower layer (subbase). In this study, the position factor (i_p) proposed by Sridharan et al. was used to overcome this shortcoming [41]. It was defined as the ratio of the Boussinesq stress influence factor at the mid-point of each layer (I_i) to the sum of the influence factor of each layer (ΣI_i). The equivalent modulus of elasticity (E_{eq}) can then be estimated by the suggested relation given by:

$$E_{eq} = \left(\frac{E_{base}^{1/3} h_{base} i_{p(base)} + E_{subbase}^{1/3} h_{subbase} i_{p(subbase)}}{h_{base} i_{p(base)} + h_{subbase} i_{p(subbase)}} \right)^3 \quad (3)$$

where, $i_{p(base)}$ is the position factor of the base layer, $= I_{base} / (I_{base} + I_{subbase})$; $i_{p(subbase)}$ is the position factor of the subbase layer, $= I_{subbase} / (I_{base} + I_{subbase})$; I_{base} is the Boussinesq stress influence factor at mid-point of base layer; and $I_{subbase}$ is the the Boussinesq stress influence factor at the mid-point of subbase layer. For the cyclic plate load test, the stress influence factor of a uniformly loaded circular area was used to calculate the position factor for the base and subbase layers. The corresponding equivalent moduli of elasticity for the various sections were presented in Table 10. For the rolling wheel load test, the shape of the applied load can be approximated by two 6-in. (152-mm) apart uniformly loaded rectangular areas (Figure 16). The stress influence factor beneath the center of the rectangle was used to calculate the position factor for the base and subbase layers. Again, the corresponding equivalent moduli of elasticity for the various sections are presented in Table 10.

Figure 37 and Figure 38 show that the BCS/slag+LTS and BCS/fly ash+LTS sections have much better rutting performance than any other sections. By comparing the rutting performance of different sections (Figure 37 and Figure 38) with the equivalent modulus of elasticity of the base and subbase layers (Table 10), one can notice that without considering the relative position of the base and subbase layers, the equivalent modulus of elasticity [equation (2)] is not able to distinguish the performance of BCS/slag+LTS and BCS/fly ash+LTS sections from other sections. However, by introducing the position factor, the modified equivalent modulus of elasticity [equation (3)] enables us to recognize the reason behind the superior rutting performance of BCS/slag+LTS and BCS/fly ash+LTS sections, as compared to the other sections. As such, one can realize that the equivalent modulus of elasticity irrespective of the relative position of individual layers [equation (2)] is not a good

performance indicator of the pavement sections. However, it can be turned into a good performance indicator by introducing the position factors [equation (3)].

Table 10
Equivalent modulus of elasticity of base and subbase layer

Section	1	2	3	4	5	6	7
	BCS + LTS	BCS/fly ash + LTS	BCS/slag + LTS	LS + LTS	LS + CTS	100%RAP/FA + CTS	50%RAP50%SC/FA + CTS
E_{eq} (MPa) ¹	269	286	354	190	361	324	335
E_{eq} (MPa) ²	401	440	603	233	314	258	275
E_{eq} (MPa) ³	407	447	615	234	312	256	273

¹ equivalent modulus of elasticity irrespective of the relative position; ² equivalent modulus of elasticity for cyclic plate load test; ³ equivalent modulus of elasticity for rolling wheel load test.

Comparison of Raw BCS, BCS/Fly ash, and BCS/Slag Base with Limestone

Base. Pavement test sections 1, 2, 3, and 4 have the same subbase material, LTS, with various base course materials. As shown in Figure 37 and Figure 38, both the fly ash and slag stabilized BCS base test sections (sections 2 and 3) performed much better than the limestone base test section (section 4) under both the cyclic plate load test and the rolling wheel load test. It is noted that the raw BCS base section, which ranks third in the equivalent modulus of elasticity, had the worst performance. Considering the poor water susceptibility of raw BCS, this inferior field performance is understandable under a wet Louisiana condition. The DCP data of the BCS base layer presented in Table 9 also shows inconsistent results as compared to its performance. This may be explained by the previous finding that the strength of the raw BCS only depends on its final moisture content [32]. Combining both the previous and the current research findings, one can conclude that the 120 grade GGBFS-stabilized BCS is a good candidate as an alternative to conventional stone base [32, 43].

Comparison of 100%RAP/FA and 50%RAP50%SC/FA Base with Limestone

Base. Pavement test sections 5, 6, and 7 have the same subbase material, CTS, with various base course materials. As shown in Figure 37 and Figure 38, the 50%RAP50%SC/FA base test section (section 7) has a rutting performance nearly comparable or slightly inferior to the limestone base test section (section 5) under both the cyclic plate load test and the rolling wheel load test. On the other hand, while the 100%RAP/FA base test section (section 6) has a rutting performance comparable to the limestone base test section under the rolling wheel load, it has significantly inferior field rutting performance under the cyclic plate load test. It should be noted here that the cyclic plate load test was performed one year after the rolling wheel load test (Table 2), and the locations of cyclic plate load test and rolling wheel load

test were close to each other (Figure 17). Extensive cracking was developed on the surface of 100%RAP/FA+CTS test section after the rolling wheel load test. The water can easily seep through the cracks down to the base layer and weaken the section. Further discussions on the comparison of the performance of the foamed asphalt stabilized RAP base sections and the limestone base sections under rolling wheel load test in terms of cracking failure can be found elsewhere [43].

Comparison of Lime Treated Soil and Cement Treated Soil. Pavement test sections 4 and 5 have the same base material, crushed limestone, with various subbase course materials. As shown in Figure 38, the lime treated soil subbase test section (section 4) has an inferior rutting performance compared to the cement treated soil subbase test section (section 5) under the rolling wheel load. On the other hand, both test sections have comparable rutting performance under the cyclic plate load (Figure 37). This observation is consistent with the DCP data in Table 9. It seems that the lime treated soil (section 4) achieved comparable strength to the cement treated soil after years. However, the lime treated soils in the other sections do not show the same observation. This may be due to the deviation in mixing and compaction of the lime treated soil and the possible leaching of the lime with time under the high water table in Louisiana. More studies are needed to better understand the long-term field performance of cementitiously stabilized soil.

Cyclic Plate Load Tests versus Rolling Wheel Load Tests

As shown in Figure 37 and Figure 38, the responses of pavement sections under the cyclic plate load were stiffer than those observed under the rolling wheel load. In this study, the rut depths caused by rolling wheel load tests were about 3 ~ 7 times (Table 11) higher than those caused by cyclic plate load tests at the number of ESALs corresponding to the rutting failure of rolling wheel load test [i.e., 0.5 in. (12.7 mm) rut depth]. There are several major factors, such as stress conditions, lateral wander, and aging effect, which can contribute to the differences in rutting performance between the cyclic plate load test and the rolling wheel load test in the study.

Table 11
The ratio of rut depth for rolling wheel load test to that for cyclic plate load test

Section	1	2	3	4	5	6	7
	BCS + LTS [#]	BCS/Flyash + LTS	BCS/Slag + LTS	LS + LTS	LS + CTS	100%RAP/FA + CTS [*]	50%RAP50%SC/FA + CTS
	N/A	5.1	6.1	7.3	6.1	N/A	3.5

[#] no test available for rolling wheel load; ^{*} failed due to cracking.

Stress Conditions. In-situ pavement stresses are mainly composed of two parts: initial in-situ stresses and stresses induced due to rolling wheel loads. Under the unidirectional rolling wheel load, a pavement element within the plane of the wheel track will experience various combinations of vertical, horizontal, and shear stresses with an extension-compression-extension multiple stress path and continuous rotation of the principal stresses, as shown in Figure 39a. On the other hand, under the cyclic plate load, various magnitudes of vertical and horizontal stresses are experienced by a pavement element beneath the center of the loading plate with a single compression stress path, as shown in Figure 39b. There is no rotation of principal stresses under the cyclic plate load. The lack of stress rotation represents a fundamental difference between the cyclic plate load test and the rolling wheel load test. This might raise some concern about the effectiveness of the traditional cyclic triaxial load tests, without rotation of principal stresses, on characterizing the pavement sections. Accordingly, various advanced laboratory equipment, such as a cyclic hollow cylinder apparatus, has been developed to better simulate the actual field conditions [25]. However, the complexity of an advanced apparatus can limit its use in practice. The best approach to overcome the difference in stress path is to develop a “correction factor” to account for the principal stress rotation. Pavement engineers can then base their designs on traditional cyclic triaxial load tests with the application of a correction factor to take into consideration the effect of principal stress rotation on the permanent deformation of pavement sections.

In addition, the friction between the tire and pavement during the rolling wheel load test results in interface tangential forces, which are not applied in the cyclic plate load test. These tangential forces induce primarily shear stress and, therefore, may result in an increase in shear flow-induced rut depth [44].

Lateral Wander Effect. Under the rolling wheel load, the LS+LTS and the 50%RAP50%SC/FA+CTS sections were failed due to a large shear flow developed in the base layer [8]. The upward (bulge) and downward (depression) displacement of the pavement surface was observed during the rolling wheel load test. The pavement surface moved downward when the wheel passed directly over the point and upward when the wheel passed along the path close to it by wander. This is an indication that the particles in the base layer experienced lateral movement (anti-shakedown), which resulted in the reduction of the bearing capacity of the base layer, and thus caused the shear failure of the base layer (similar to the general shear failure in foundation application). This might explain why the LS+LTS section, which has an equivalent modulus of elasticity just slightly lower than the 100%RAP/FA+CTS and the 50%RAP50%SC/FA+CTS sections (Table 10), had much worse

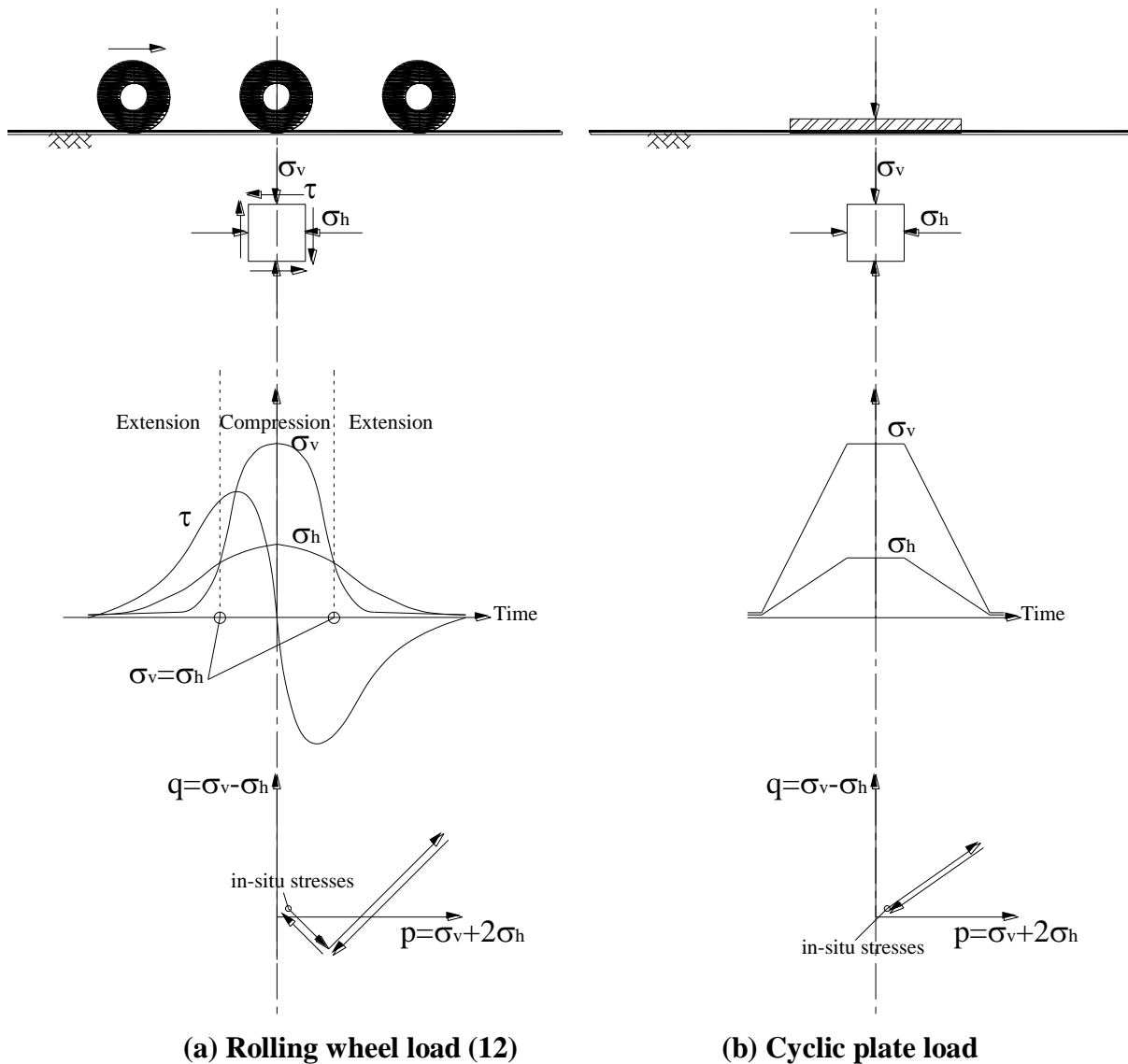


Figure 39
Stress regimes experienced by pavement element under two types of loading

performance under rolling wheel load (Figure 38). For the 50%RAP50%SC/FA base material, although it was stabilized with asphalt binder, the use of only 2.8 percent asphalt cement content was not able to bond the aggregate skeleton effectively at the design air void of 20.3 percent. As such, the 50%RAP50%SC/FA base material experienced an initial shakedown or consolidation (i.e., further densification) with possible bond breaking due to the tensile force induced by the particle movement. After 241,000 ESALs, a dramatic increase in permanent deformation occurred due to the gradual reduction in the bearing capacity of the material from lateral wander-induced particle rearrangement. On the other

hand, the cyclic plate load caused the unbound/bound base layers to consolidate and shakedown to a steady state, as shown in Figure 37.

For the BCS/slag+LTS section under the rolling wheel load, the load after 1,048,019 ESALs was increased to 16,650 lb. (74.1 kN). Under such a high load with many loading repetitions and lateral wander effect, the BCS/slag base layer reached an incremental collapse range of shakedown after 3,684,000 ESALs. At this stage, the BCS/slag+LTS material experienced an excessive permanent deformation [jump from 0.2 in. (5.1 mm) to 0.5 in. (12.7 mm)].

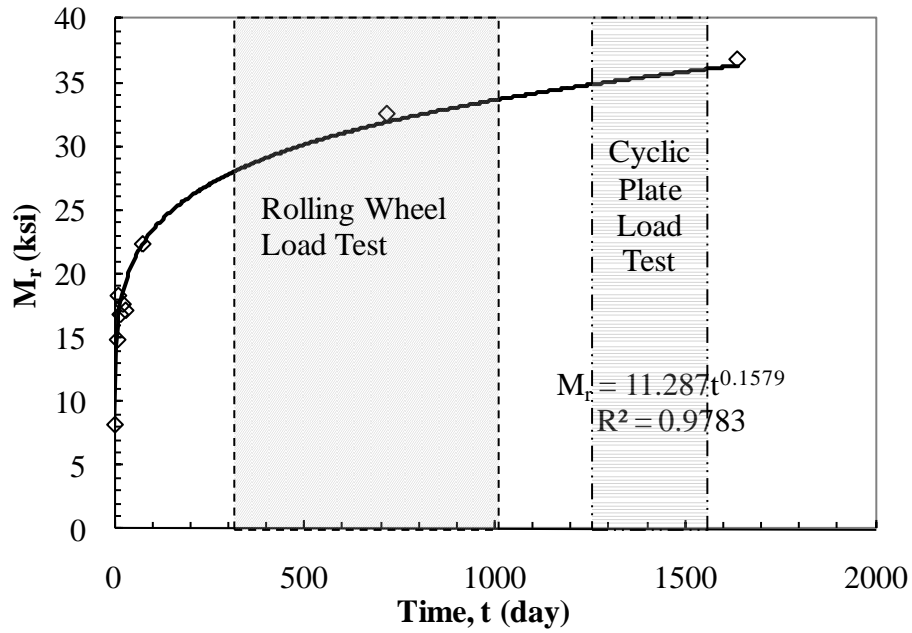
Aging Effect. It should be mentioned that the construction of all test sections was completed in December of 2004. The rolling wheel load test started in October 2005 for sections 2, 3, and 7 and in January 2007 for sections 4, 5, and 6. The cyclic plate load tests were conducted at least 10 months after the end of the rolling wheel load tests (Table 2). Some of the tests were even performed more than two years after the end of the rolling wheel load tests (e.g., sections 2, 3, and 7). The strength of cementitiously stabilized soils generally increases with time through pozzolanic reactions. The mean values of the resilient modulus, M_r , for the lime treated soil and the cement treated soil at different times are shown in Figure 40. The resilient moduli were obtained using the CBR-DCPI relationship suggested by Webster et al. and the M_r -CBR relationship suggested by Powell et al. [45, 46].

$$\left. \begin{aligned} CBR &= 292/(DCPI)^{1.12} \\ M_r(psi) &= 2555 \times CBR^{0.64} \end{aligned} \right\} \rightarrow M_r(psi) = 96658/(DCPI)^{0.7168} \quad (4)$$

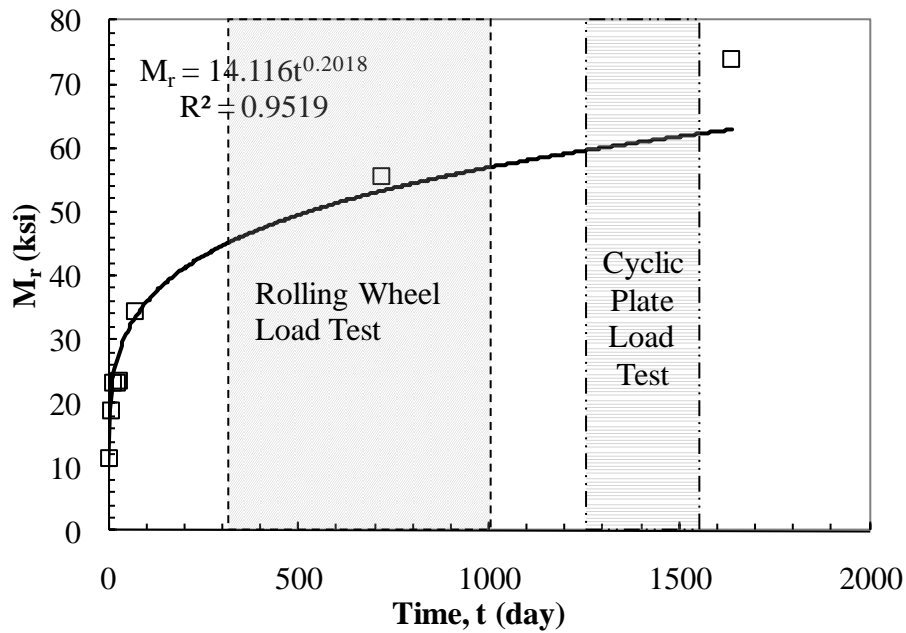
As can be seen from the figure, the resilient modulus, M_r , for the lime/cement stabilized soil layer increased exponentially with time. This means that the strength/stiffness of the lime/cement treated soils increased rapidly during the early stages of curing time and continues to increase at a slower rate after that. The increase of M_r with time (age effect) of the treated and stabilized bases/subbases in the test sections partially contributed to the differences between the rolling wheel tests and the cyclic plate load tests that were performed at least 10 months later.

As mentioned earlier, two similar pavement sections, with limestone base and lime treated soil subbase, were constructed: one at the Louisiana Pavement Research Facility site and the other in a steel box at the LTRC GERL laboratory. While the lime treated subbase soil in the field test section aged more than three years before the start of cyclic plate load, the lime treated subbase soil in the laboratory test section only aged about three months. The difference in response between the field and laboratory cyclic plate load test (i.e., the stiffer

response of field test section), as shown in Figure 36, clearly demonstrates the effect of aging on the performance of pavement test sections.



(a) Lime treated soil



(b) Cement treated soil

Figure 40
Variation of the resilient modulus M_r with time

General Comments

Although Figure 37 and Figure 38 show that the responses of pavement test sections under cyclic plate load were stiffer than those obtained under rolling wheel load, the performance of different pavement sections is generally in the same order under both loadings. In other words, the result of the cyclic plate load test may overestimate the rutting performance of the pavement test sections, but it can be a good performance indicator for the evaluation of the different pavement structures. As such, the laboratory cyclic plate load test, which is faster and cost much less than the field rolling wheel test, can be used for comparing the performance of different test sections and for pre-selecting test sections for field testing.

CONCLUSIONS

An indoor cyclic plate load testing equipment was developed, as part of this study, for use to evaluate the performance of pavement sections with different base materials, different subgrade conditions, different cross sections, as well as to evaluate new materials, new stabilizing techniques, and new design methodologies. The testing equipment was used to conduct a series of in-box tests aimed at evaluating the performance and benefits of geogrid base reinforcement in flexible pavement sections over weak subgrade soils. The testing equipment was also deployed to the PRF site for full-scale testing to evaluate the performance of different base/subbase materials in pavement sections and to compare the pavement response under the cyclic plate load test with that using the rolling wheel load test. The following sections will summarize the conclusions made from these two testing programs.

The research study also included conducting laboratory testing to evaluate the performance of geogrid reinforced base course specimens under repeated load testing using an MTS machine, and performing numerical parametric study to investigate the benefits of geogrid base reinforcements in flexible pavement structures. The conclusions from these studies were published in Report No. FHWA/LA.09/450 [1].

Evaluation of Geogrid Base Reinforcement Using Cyclic Plate Load Test

In-box cyclic plate load tests were conducted to investigate the potential benefits of using geogrid base reinforcement in flexible pavements. The influences of various parameters contributing to the improved performance of flexible pavement with geogrid base reinforcement were examined. This included the tensile modulus, aperture shape (geometry), and location of geogrid reinforcement. Also, an instrumentation program was designed to investigate the stress distribution, permanent vertical strain, and the development of pore water pressure in the subgrade layer and the strain distribution along the geogrid reinforcement.

Based on the test results of the cyclic plate load tests on pavement sections with and without geogrid base reinforcement, the following conclusions can be drawn:

- The inclusion of geogrid for base reinforcement can significantly reduce the rut depth and extend the service life of pavement sections built on weak subgrades. The traffic benefit ratio, TBR, can be increased up to 15 at a rut depth of 0.75 in. (19 mm) for pavement constructed using a 12-in. (305-mm) thick base course layer over weak subgrade soil with $\text{CBR} \leq 1$ percent.

- The improvement in performance of the geogrid base reinforcement is in the same order as to the increase of the geogrid tensile modulus. At a rut depth of 0.75 in. (19 mm), the TBR increased from 5.5 for the biaxial geogrid GG1 to 6.1 for the biaxial geogrid GG2, of a higher tensile modulus. Meanwhile, the TBR increased from 6.4 for the triaxial geogrid GG3 to 7.4 for the triaxial geogrid GG4, which has a higher tensile modulus.
- The triaxial geogrids with triangular aperture geometry performed better than biaxial geogrids with rectangular aperture geometry. At a rut depth of 0.75 in. (19 mm), the TBR increased from 5.5 for the biaxial geogrid GG1 to 6.4 for the triaxial geogrid GG3. Meanwhile, the TBR increased from 6.1 for the biaxial geogrid GG2 to 7.4 for the triaxial geogrid GG4.
- The inclusion of geogrids in pavements results in redistributing the applied load to a wider area, thus reducing the stress concentration and achieving an improved vertical stress distribution on top of the subgrade layer. This behavior will reduce the accumulated permanent deformation within the subgrade.
- Better performance was observed when the geogrid layer was placed at the upper one third of the base course layer thickness than that when the geogrid was placed at the base-subgrade interface or at the middle of the base layer.
- The construction method can have a significant effect on mobilizing the interaction between the geogrid and base course aggregates. Better interlocking can be achieved by placing the geogrid on top of a loose aggregate layer [2 in. (51 mm) thick in compacted state], sandwiching it by another layer of loose aggregate [4 in. (102 mm) thick in compacted state], and then compacting both layers together. A better geogrid-base interaction can also be achieved by applying a prime coat to the surface of the support layer before placing the geogrid, which believed to promote the bonding between the geogrid layer and the base aggregate materials in the support and confined layers.
- The strength of the subgrade is a very important factor in the performance of geogrid base reinforcement in pavement sections.
- The bondable foil strain gages, which experience both accumulation of plastic strain and relatively high dynamic strain level, are not suitable for continuous monitoring the strain development along the geogrid under cyclic loading tests, especially for high numbers of load cycles. New durable instrumentation needs to be developed to measure the strain distribution along the geogrid reinforcement under cyclic loading.

Field Tests on Various Base/Subbase ALF Test Lanes

Full-scale field tests were conducted on seven test lane sections built at the PRF site to evaluate the performance of pavement sections with different base/subbase materials. Two types of loading were used for comparison, the cyclic plate load test and the rolling wheel load test. The tested sections include BCS, stabilized BCS, stabilized RAP, and stabilized soil as base/subbase materials. The differences in pavement responses to cyclic plate load and rolling wheel load were investigated. Based on the results of this study, the following conclusions can be drawn:

- The rut depths resulted from the rolling wheel load tests, in all test sections, were much higher than those obtained from the cyclic plate load tests. The differences were as much as 3 ~ 7 times between these two types of loading. This indicates that the rolling wheel load produces much more damaging loading condition than the cyclic plate load. Three possible factors can attribute to the difference in pavement responses under these two types of loading conditions: principal stress rotation, friction induced tangential forces, and lateral wander. The extension-compression-extension multiple stress path type test with principal stress rotation (rolling wheel test) causes a much higher permanent deformation than the single compression stress path type test with no principal stress rotation (cyclic plate load test). The lateral wander most likely decreases the stability of unbound and weak bound granular base materials by inducing lateral particle movement. As such, a correction factor is needed to account for the differences between the rolling wheel load test and the cyclic plate load test.
- The resilient modulus, M_r , of the stabilized/treated soil increases rapidly during the early stages of curing time and continues to increase at a slower rate thereafter. The authors believe this age effect partially contributes to the differences between the rolling wheel load tests and the cyclic plate load tests, which were performed at least 10 months after rolling wheel load tests.
- The performance responses of the different test sections under cyclic plate load tests are in the same order as that under rolling wheel tests. Therefore, the cyclic plate load test can be used as a good performance indicator test for evaluating and comparing the performance of different pavement sections, and for pre-selecting and screening of test sections for further full-scale field tests.
- The use of a conventional formula to calculate the equivalent modulus of elasticity, in which only the thickness of individual layers is considered, is not a good performance indicator for the design of multi-layer pavement systems. The modified formula proposed

in this study using the position factor (i_p) based on Boussinesq stress distribution in soil provides the means to overcome this shortcoming. The formula was successfully used to evaluate the performance of the pavement sections tested in this study, and to demonstrate that the modified formula for equivalent modulus of elasticity is a good performance indicator.

- The performance of 120 grade GGBFS stabilized BCS as a base material is superior compared to the conventional stone base material, and therefore, is a good candidate as an alternative to the conventional stone base.
- The two foam asphalt stabilized RAP base materials tested in this study did not perform well as compared to the other sections. The development of new stabilization schemes for RAP is therefore needed.

RECOMMENDATIONS

Based on the results of this research study, which includes laboratory testing of geogrid-reinforced base aggregate specimens, indoor cyclic plate load testing on geogrid base reinforced pavement sections, full-scale field testing on several base/subbase materials pavement sections, and the finite element analyses to investigate the benefits of geogrid base reinforcements in flexible pavement, the following recommendations are offered to LADOTD:

- The cyclic plate load test can be used as a good performance indicator test for evaluating pavement sections. Therefore, researchers recommend using the in-box cyclic plate testing equipment effectively for pre-selection of pavement sections prior to full-scale field testing to save time and cost when the load-related performance of new pavement materials and concepts are needed to be evaluated and approved.
- It is recommended that the LADOTD pavement design engineers consider reinforcing the base course aggregate layer with one or two geogrid layers in the design of flexible pavements built on soft subgrades with resilient modulus $M_r < 2000$ psi (13,790 kN/m²) (or CBR value < 1.5), especially in cases where it is difficult to stabilize/treat the soft subgrade soil with cement or lime and to create working platforms for constructing pavements and embankments on soft soils. The use of geogrids with elastic tensile strength at 2 percent strain, $T_{2\%} \geq 250$ lb/ft (3.65 kN/m), is recommended.
- For flexible pavements built on top of soft subgrades (or to create a working platform), researchers recommend placing one layer of geogrid at the base-subgrade interface (stabilization layer) immediately above the non-woven geotextile for a base course thickness of equal or less than 18 in. (457.2 mm). For base thicknesses greater than 18 in. (457.2 mm), two geogrid layers are recommended, one layer to be placed at base-subgrade interface and another geogrid layer within the upper one third of the base course layer.
- It is strongly recommended to consider using geogrids (and high strength geotextiles) in widening existing roadways through stabilizing weak subgrade layers. The inclusion of geogrid/geotextile layer at the base-subgrade interface will improve the bearing capacity of the subgrade layer, increases its resistance to shear failure, and helps eliminating the differential settlement between the existing and new lanes. The DCP test can be used to evaluate the strength condition and resilient modulus of the subgrade soil for use as input parameters in the design the new pavement lane section.

- Researchers recommend using the proposed modified equivalent formula to calculate the equivalent modulus of elasticity, which considers both the thickness and relative position of individual layers, in the design and analysis of pavements when multi-layers have to be combined from a practical standpoint.
- Full-scale field tests on pavement sections with geogrid base reinforcement (e.g., using rolling wheel load testing facility at the Louisiana Pavement Research Facility Site) should be conducted to verify/validate the findings of this research. This will also provide the opportunity to monitor the performance of geogrid base reinforcement in pavements under field conditions.
- Additional research study is needed to characterize the effect of geogrid-aggregate interlocking and geogrid-subgrade interface on the performance of geogrid base reinforcement/ subgrade stabilization in flexible pavement structures, and to evaluate the extent of the influenced zone adjacent to the geogrid layer.

ACRONYMS, ABBREVIATIONS, AND SYMBOLS

AASHTO	American Association of State Highway and Transportation Officials
AC	asphalt concrete
ALF	accelerated loading facility
ASTM	American Standard for Testing Materials
BCS	blended calcium sulfate
BNC	Bayonet Neill-Concelman
CBR	California bearing ratio
CTS	cement treated soil
CV	coefficient of variation
DCP	dynamic cone penetrometer
DCPI	dynamic cone penetrometer index
ESAL	equivalent single axel load
FA	foamed asphalt
FHWA	Federal Highway Administration
ft.	foot (feet)
FWD	falling weight deflectometer
GG	Geogauge
GGBFS	ground granulated blast furnace slag
HMA	hot-mix asphalt
in.	inch(es)
kip	kilo pounds
kN	kilonewton
kpa	kilopascal
ksi	kilo pounds per square inch
LADOTD	Louisiana Department of Transportation and Development
lb.	pound(s)
LFWD	light falling weight deflectometer
LL	liquid limit
LTRC	Louisiana Transportation Research Center
LTS	lime treated soil
LVDT	linear variable displacement transducer
m	meter(s)
MEPDG	mechanistic-empirical pavement design guide
mm	millimeter(s)
MPa	megapascal

pcf	pounds per cubic feet
PG	Performance graded
PI	plasticity index
PRF	pavement research facility
psi	pounds per square inch
PSPA	portable seismic pavement analyzer
RAP	recycled asphalt pavement
TRB	traffic benefit ratio
UCS	unconfined compressive strength
USCS	Unified Soil Classification System

REFERENCES

1. Abu-Farsakh, M., and Nazzal, M., *Evaluation of the Base/Subgrade Soil under Repeated Loading: Phase I– In-Box and ALF Cyclic Plate Load Tests*, Final Report. No. FHWA/LA.09/450, Louisiana Transportation Research Center, Baton Rouge, LA, 2009. 77 pp.
2. ARA, Inc., ERES Consultants Division, “Guide for Mechanistic-Empirical Design of New and Rehabilitated Pavement Structures.” <http://www.trb.org/mepdg/guide.htm>. 2004.
3. Al-Qadi, I.L., Brandon, T.L., and Bhutta, S.A., “Geosynthetic Stabilized Flexible Pavements.” *Proceedings of the Conference Geosynthetics '97*, Long Beach, CA, USA, March, 1997, 1997. pp. 647-661.
4. Cancelli, A., and Montanelli, F., “In-ground Test for Geosynthetic Reinforced Flexible Paved Roads.” *Proceedings of the Conference Geosynthetics '99*, Boston, MA, USA, April, 1999. pp. 863-878.
5. Wasage, T.L.J, Ong, G.P., Fwa, T.F., and Tan, S.A., “Laboratory Evaluation of Rutting Resistance of Geosynthetics Reinforced Asphalt Pavement.” *Journal of the Institution of Engineers, Singapore*, Vol. 44, No. 2, 2004. pp. 29-44.
6. Montanelli, F., Zhao, A., and Rimoldi, P., “Geosynthetic-reinforced Pavement System: Testing & Design.” *Proceedings of the Conference Geosynthetics '97*, Long Beach, CA, USA, March, 1997, 1997. pp. 619-632.
7. Moghaddas-Nejad, F., and Small, J.C., “Effect of Geogrid Reinforcement in Model Track Tests on Pavements.” *Journal of Transportation Engineering*, Vol. 122, No. 6, 1996. pp. 468-474.
8. Kinney, T.C., Abbott, J., and Schuler, J., “Benefits of Using Geogrids for Base Reinforcement with Regard to Rutting.” *Transportation Research Record: Journal of the Transportation Research Board*, No. 1611, National Research Council, 1998. pp. 86-96.
9. American Association of State Highway and Transportation Officials (AASHTO), *AASHTO Guide for Design of Pavement Structures*, Washington, DC. 1993.

10. Hass, R., Walls, J., and Carroll, R.G., "Geogrid Reinforcement of Granular Bases in Flexible Pavements." In *Transportation Research Record 1188* Transportation Research Board, National Research Council, Washington, D.C., 1988. pp. 19-27.
11. Al-Qadi, I.L., Barndon, T.L., Valentine, R.J., Lacina, B.A., and Smith, T.E., "Laboratory Evaluation of Geosynthetics Reinforced Pavement Sections." *Transportation Research Record: Journal of the Transportation Research Board*, No. 1439, 1994. pp. 25-31.
12. Perkins, S.W., "Geosynthetic Reinforcement of Flexible Pavements Laboratory Based Pavement Test Sections." *Federal Highway Administration Report FHWA/MT-99-001/8138*, Montana Department of Transportation, Helena, Montana, USA, 1999. 109 pp.
13. Perkins, S.W., "Mechanistic-empirical Modeling and Design Model Development of Geosynthetic Reinforced Flexible Pavements." *Federal Highway Administration Report FHWA/MT-01-002/99160-1A*, Montana Department of transportation, Helena, Montana, USA, 2001. 126 pp.
14. Perkins, S.W., "Evaluation of Geosynthetic Reinforced Flexible Pavement Systems Using Two Pavements Test Facilities." *Federal Highway Administration Report FHWA/MT-02-008/20040*, Montana Department of Transportation, Helena, Montana, USA, 2002. 120 pp.
15. Berg, R. R., Christopher, B.R., and Perkins, S.W., "Geosynthetic Reinforcement of the Aggregate Base Course of Flexible Pavement Structures." *GMA White paper II*, Geosynthetic Materials Association, Roseville, MN, USA, 2000. 100 pp.
16. Collin, J.G., Kinney, T.C., and Fu, X., "Full Scale Highway Load Test of Flexible Pavement System with Geogrid Reinforced Base Courses." *Geosynthetics International*, Vol. 3, No. 4, 1996. pp. 537-549.
17. Webster, S.L., "Geogrid Reinforced Base Courses for Flexible Pavements for Light Aircraft: Test Section Construction, Behavior Under Traffic, Laboratory Tests, and Design Criteria." *Technical Report GL-93-6*, USAE Waterways Experiment Station, Vicksburg, MS, USA. 1993. 86 pp.
18. Al-Qadi, I.L., Dessouky, S.H., Kwon, J., and Tutumluer, E., "Geogrid in Flexible Pavements: Validated Mechanism." *Transportation Research Board 2008 Annual Meeting CD-ROM*. 2008.

19. Van Deusen, D.A., Newcomb, D.E., and Labuz, J.F., "A Review of Instrumentation Technology for the Minnesota Road Research Project." *Federal Highway Administration Report FHWA/MN/RC-92/10*, Minnesota Department of Transportation, 1992. 120 pp.
20. Brown, S.F., and Brodrick, B.V., "25 Years' Experience with the Pilot-scale Nottingham Pavement Test Facility." *Proceedings of International Conference on Accelerated Pavement Testing*, Reno, Nevada, October 1999. pp. 18-20.
21. Hornych, P., Kazai, A., and Quibel, A., "Modeling a Full Scale Experiment of Two Flexible Pavement Structures with Unbound Granular Bases." In *Unbound Aggregates in Road Construction*, A.A. Balkema, Leiden, Netherlands, 2000. pp. 359-367.
22. Crockford, W.W., "Role of Principal-plane Rotation in Flexible Pavement Deformation." *Journal of Transportation Engineering*, Vol. 119, No. 1, 1993. pp. 124-141.
23. Kim, T., and Tutumluer, E., "Unbound Aggregate Rutting Models for Stress Rotations and Effects of Moving Wheel Loads." *Transportation Research Record: Journal of Transportation Research Board*, No. 1913, 2005. pp. 41-49.
24. Kim, T., and Tutumluer, E., "Field Validation of Airport Pavement Granular Layer Rutting Predictions." *Transportation Research Record: Journal of Transportation Research Board*, No. 1952, 2006. pp. 48-57.
25. Grabe, P.J., and Clayton, C.R.I., "Effects of Principal Stress Rotation on Permanent Deformation in Rail Track Foundations." *Journal of Geotechnical and Geoenvironmental Engineering*, Vol. 134, No. 4, 2009. pp. 555-565.
26. White, T.D., Hua, J., and Galal, K., "Analysis of Accelerated Pavement Tests." *Proceedings of the First International Conference on Accelerated Pavement Testing (CD-ROM)*, Reno, NV, Oct. 18-20. 1999.
27. Epps, A.L., Ahmed, T., Little, D.C., and Hugo, F., *Performance Prediction with the MMLS3 at WesTrack*, Final Report. Texas Transportation Institute, The Texas A&M University, College Station, TX, Report No. FHWA/TX-01/2134-1, 2001. 132 pp.
28. White, T.D., Haddock, J.E., and Hand, A.J.T., and Fang, H., *NCHRP Report 468: Contributions of Pavement Structural Layers to Rutting of Hot Mix Asphalt*, National

Cooperative Highway Research Program, Transportation Research Board, National Research Council, Washington, D.C. 2002. 151 pp.

29. Donovan, P., and Tutumluer, E., “Effect of Aircraft Load Wander on Unbound Aggregate Pavement Layer Stiffness and Deformation Behavior.” *Proceedings of the 2008 Airfield and Highway Pavements Conference*, Oct. 15-18, Bellevue, Washington, American Society of Civil Engineers (ASCE), Reston, VA, 2008. pp. 465-476.
30. Mohammad, L.N., Abu-Farsakh, M., Wu, Z., and Abadie, C., “Louisiana Experience with Foamed Recycled Asphalt Pavement Base Materials.” *Transportation Research Record: Journal of Transportation Research Board*, No. 1832, 2003. pp. 17-24.
31. Romanoschi, S., Hossain, M., Heitzmann, M., and Gisi, A., “Accelerated Pavement Testing Evaluation of the Structural Contribution of Full-depth Reclamation Material Stabilized with Foamed Asphalt.” *Transportation Research Record: Journal of Transportation Research Board*, No. 1896, 2004. pp. 199-207.
32. Tao, M., and Zhang, Z., “Enhanced Performance of Stabilized By-product Gypsum.” *Journal of Materials in Civil Engineering*, ASCE, Vol. 17, No. 6, 2005. pp. 617-623.
33. Zhang, Z., and Tao, M., *Stability of Calcium Sulfate Base Course in a Wet Environment*, Final Report. No. FHWA/LA.06/419, Louisiana Transportation Research Center, Baton Rouge, LA, 2006. 77 pp.
34. Mcmanis, K., Identification and Stabilization Methods for Problematic Silt Soils: A Laboratory Evaluation of Modification and Stabilization Additives. Final Report No. FHWA/LA.02/371, Louisiana Transportation Research Center, Baton Rouge, LA, 2003. 61 pp.
35. Louisiana Department of Transportation and Development, *Louisiana Standard Specifications for Roads and Bridges*. Louisiana Department of Transportation and Development, Baton Rouge, LA. 2006.
36. Vishay Measurements Group Inc., “Catalog 500—strain Gage Technical Data.” Micro-Measurements Division, Raleigh, NC. 2003.

37. Abu-Farsakh, M., Chen, Q., Sharma, R., and Zhang, X., "Large-Scale Model Footing Tests on Geogrid Reinforced Foundation and Marginal Embankment Soil." *Geotechnical Testing Journal*, Vol. 31, No. 5, 2008. pp. 413-423.
38. Mohammad, L.N., and Herath, A., *Accelerated Loading Evaluation of A Sub-Base Layer on Pavement Performance*, Interim Report, Louisiana Transportation Research Center, Baton Rouge, LA, 2005. 54 pp.
39. Hsu, C.C., and Vucetic, M., "Threshold Shear Strain for Cyclic Pore-water Pressure in Cohesive Soils." *Journal of Geotechnical and Geoenvironmental Engineering*, Vol. 132, No. 10, 2006. pp. 1325-1335.
40. National Highway Institute, *Introduction to Mechanistic-Empirical Pavement Design: Reference Manual*, Publication No. NHI-02-048. 2002.
41. Sridharan, A., Gandhi, N.S.V.V.S.J., and Suresh, S., "Stiffness Coefficients of Layered Soil Systems." *Journal of Geotechnical Engineering*, Vol. 116, No. 4, 1990. pp. 604-624.
42. Sadrekarimi, J., and Akbarzad, M., "Comparative Study of Methods of Determination of Coefficient of Subgrade Reaction." *Electronic Journal of Geotechnical Engineering*, Vol. 14, Bund. E. 2009.
43. Wu, Z., Zhang, Z., and Morvant, M., "Performance of Various Base/Subbase Materials Under Accelerated Loading." *Transportation Research Board 88th Annual Meeting Compendium of Papers CD-ROM*, January 13-17, Washington, D.C. 2008.
44. Weissman, S.L., "Influence of Tire-pavement Contact Stress Distribution on Development of Distress Mechanisms in Pavements." *Transportation Research Record: Journal of Transportation Research Board*, No. 1655, 1999. pp. 161-167.
45. Webster, S.L., Grau, R.H., and Williams, R.R., *Description and Application of Dual Mass Dynamic Cone Penetrometer*. U.S. Army Engineer Waterways Experiment Station, Instruction Report, No. GL-92-3. 1992.
46. Powell, W.D., Potter, J.F., Mayhew, H.C., and Nunn, M.E., *The Structural Design of Bituminous Roads*. Transport and Road Research Laboratory (TRRL), Report LR1132, Berkshire, United Kingdom. 1984.